

AD-A091 674

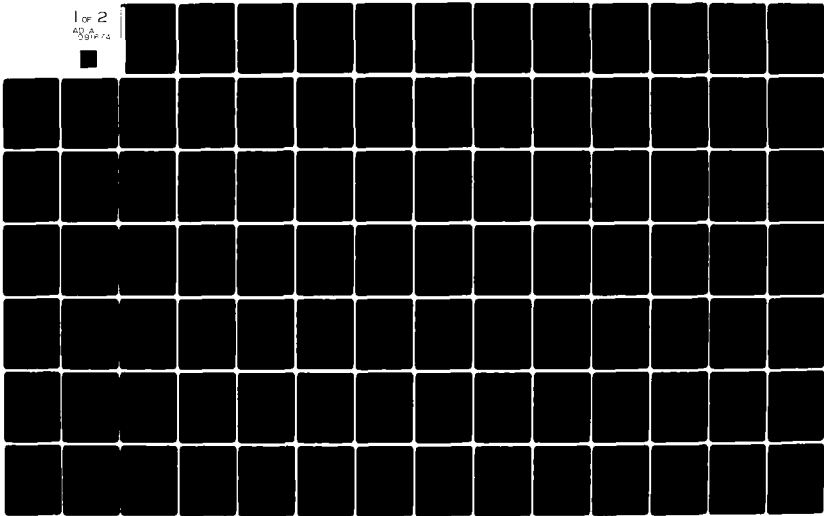
TEXAS UNIV AT AUSTIN DEPT OF AEROSPACE ENGINEERING AN--ETC F/6 1/3
THE EFFECTS OF WARHEAD-INDUCED DAMAGE ON THE AEROELASTIC CHARAC--ETC(U)
JUL 80 J H CHANG, R O STEARMAN AFOSR-78-3569

UNCLASSIFIED

AFOSR-TR-80-1039

NL

1 of 2
AFOSR-78-3569



AFOSR-TR- 80 - 1039

AFOSR TR

LEVEL II

①

AD A091674

Air Force Office of Scientific Research

Eglin Air Force Base

Grant █-AFOSR 78-3569-█

THE EFFECTS OF WARHEAD-INDUCED DAMAGE ON THE AEROELASTIC
CHARACTERISTICS OF LIFTING SURFACES
VOLUME I - AEROELASTIC EFFECTS

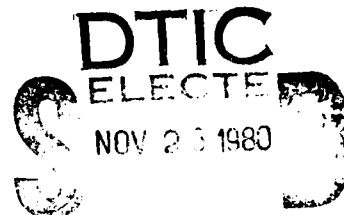
by

R. O. Stearman

and

J. H. Chang

Department of Aerospace Engineering
and Engineering Mechanics



CENTER FOR AERONAUTICAL RESEARCH

Bureau of Engineering Research
The University of Texas at Austin
Austin, Texas 78712

80 10 21 023

17. APPROVAL/ISSUANCE PAGE		READ INSTRUCTIONS BEFORE COMPLETING FORM	
1. REPORT NUMBER AFOSR-TR-80-1039	2. GOVT ACCESSION NO. AD-A091674	3. RECIPIENT'S CATALOG NUMBER 19	
4. TITLE (and subtitle) The Effects of Warhead-Induced Damage on the Aeroelastic Characteristics of Lifting Surfaces. Volume I - Aeroelastic Effects.		5. TYPE OF REPORT & PERIOD COVERED Final Technical Report 2-1-79-20-2-1-80	
6. AUTHOR(s) J. H. Chang R. O. Stearman		7. PERFORMING ORG. REPORT NUMBER 1 Feb 79 - 31 Jan 80	
8. CONTRACT OR GRANT NUMBER(s) AFOSR-78-3569		9. PERFORMING ORGANIZATION NAME AND ADDRESS Center for Aeronautical Research Dept. of Aerospace Engineering/Engr. Mechanics The University of Texas at Austin/Austin TX 78712	
10. CONTROLLING OFFICE NAME AND ADDRESS Air Force Office of Scientific Research (AFSC) Bolling Air Force Base Washington D. C. 20332		11. PROGRAM ELEMENT, PROJECT, TASK AREA & WORK UNIT NUMBERS 61102F 10-2301/V/96	
12. REPORT DATE Jul 1980		13. NUMBER OF PAGES 120	
14. MONITORING AGENCY NAME & ADDRESS (if different from Controlling Office) AFOSR LEV		15. SECURITY CLASS. (of this report) Unclassified	
16. DISTRIBUTION STATEMENT (of this Report) Approved for public release; distribution unlimited		17. DISTRIBUTION STATEMENT (of the abstract entered in Block 20, if different from Report) STIC CTED NOV 7 1980 C	
18. SUPPLEMENTARY NOTES		19. KEY WORDS (Continue on reverse side if necessary and identify by block number) Damaged Lifting Surfaces Drag Divergence Aeroelasticity & Ballistic Damage	
20. ABSTRACT (Continue on reverse side if necessary and identify by block number) An investigation is being conducted to determine whether ballistic damage can seriously degrade the aeroelastic integrity of lifting surfaces on air- craft. A potential aeroelastic failure mode that was identified in the first year's study has been investigated here over a larger range of parameters. This failure mechanism results from the localized steady drag generated when			

FILE COPY

DD FORM 1 JAN 73 1473 EDITION OF 1 NOV 65 IS OBSOLETE

Unclassified

402465 SECURITY CLASSIFICATION OF THIS PAGE (When Data Entered)

1 lifting surface encounters damage to its aerodynamic shape. Its modeling has been extended in this study to swept wing configurations and to possible multiple and distributed damage sites. In addition, a larger range of single damage site locations have also been considered to assess the possible trade-offs between the influence of both structural and aerodynamic damage locations. A check on the validity of the strip theory aerodynamic modeling employed in this study has also been made by comparing these results with those obtained from a lifting surface theory modeling.

Finally, an additional failure mechanism is identified that results from any unsteady but periodic fluctuating aerodynamic drag loads that are generated by the damage. A parametric and oscillatory instability can be induced by relatively low level drag loads in theis case if they happened to be appropriately tuned to the structural frequencies of the wing.



Air Force Office of Scientific Research

Eglin Air Force Base

Grant █-AFOSR 78-3569-█

THE EFFECTS OF WARHEAD-INDUCED DAMAGE ON THE AEROELASTIC
CHARACTERISTICS OF LIFTING SURFACES
VOLUME I - AEROELASTIC EFFECTS

by

R. O. Stearman

and

J. H. Chang

Department of Aerospace Engineering
and Engineering Mechanics

CENTER FOR AERONAUTICAL RESEARCH

Bureau of Engineering Research
The University of Texas at Austin
Austin, Texas 78712

July, 1980

AIR FORCE OFFICE OF SCIENTIFIC RESEARCH (AFSC)
NOTICE OF TRANSMITTAL TO DDC

This technical report has been reviewed and is
approved for public release IAW AFR 190-12 (7b).
Distribution is unlimited.

A. D. BLOSE
Technical Information Officer

ACKNOWLEDGMENTS

This research was sponsored by Vulnerability Assessments Group of the Air Force Office Armament Laboratory, Eglin Air Force Base, through the Air Force Office of Scientific Research. Mr. J. M. Heard was technical monitor of the program, carried out under Grant #AFOSR 78-3569, during the period 1 February 1979 through 31 January 1980.

Accession No.	
NTIS GRA&I	<input checked="" type="checkbox"/>
DTIC T&S	<input type="checkbox"/>
Unannounced	<input type="checkbox"/>
Justification	
By	
Distribution	
Availability	Colon
Area	AFSC/AFSC
Dist	Special

R

THE INFLUENCE OF BALLISTIC DAMAGE ON THE
AEROELASTIC CHARACTERISTICS OF LIFTING SURFACES

J. H. Chang*

R. O. Stearman**

ABSTRACT

An investigation is being conducted to determine whether ballistic damage can seriously degrade the aeroelastic integrity of lifting surfaces on aircraft. A potential aeroelastic failure mode that was identified in the first year's study has been investigated here over a larger range of parameters. This failure mechanism results from the localized steady drag generated when a lifting surface encounters damage to its aerodynamic shape. Its modeling has been extended in this study to swept wing configurations and to possible multiple and distributed damage sites. In addition, a larger range of single damage site locations have also been considered to assess the possible trade-offs between the influence of both structural and aerodynamic damage locations. A check on the validity of the strip theory aerodynamic modelling employed in this study has also been made by comparing these results with those obtained from a lifting surface theory modeling.

*Graduate student, Aerospace Engineering and Engineering Mechanics Dept., The University of Texas at Austin, Austin, Texas.

**Professor of Aerospace Engineering and Engineering Mechanics, The University of Texas at Austin, Austin, Texas.

Finally, an additional failure mechanism is identified that results from any unsteady but periodic fluctuating aerodynamic drag loads that are generated by the damage. A parametric and oscillatory instability can be induced by relatively low level drag loads in this case if they happened to be appropriately tuned to the structural frequencies of the wing.

TABLE OF CONTENTS

	<i>Page</i>
ACKNOWLEDGMENTS	i
ABSTRACT	ii
TABLE OF CONTENTS	iv
LIST OF TABLES	v
LIST OF FIGURES	vii
TEXT	1
1. Introduction	1
2. Damage Identification	5
2.1 Structural Damage Modelling	5
2.2 Aerodynamic Damage Modelling	7
3. Damage Influence on Flutter and Divergence Speeds of a Zero Sweep Statistical Fighter Wing	18
4. Damage Influence on the Flutter and Divergence of Swept Wings	22
5. Influence of Distributed and Multiple Damage Site Drag Effects on Flutter and Divergence of Swept Wings	25
6. Comparison of the Previous Strip Theory Drag Divergence Modelling with a Lifting Surface Theory Modelling	27
7. Significance of Damage Induced Unsteady Drag Effects on Promoting Failure of Lifting Surfaces	31
8. Conclusions	31

TABLE OF CONTENTS (continued):		Page
REFERENCES	• • • • • • • • • • • • • • •	33
FIGURES	• • • • • • • • • • • • •	35
TABLES	• • • • • • • • • • •	50
APPENDIXES	• • • • • • • • • • •	88
Appendix A - Estimate of Drag Increments Due to Damage	• • • • • • • •	88
Appendix B - Problem Formulation	• • • • •	96
Appendix C - Finite Element Modeling of Structural Damage	• • • • • • •	100

LIST OF TABLES

	<i>Page</i>
Table 1. Statistical Fighter Properties Determined as Geometric Means of the Fourteen Different Fighter Aircraft	50
Table 2. Typical Date Sheet for Determination of Para- meters for Representative Airplane - Class I. .	51
Table 3. Key to Generalized Damage Classes	53
Table 4. Damage-Induced Drag Levels for Various Maneuvering Fight Conditions	54
Table 5. First Six Uncoupled Vibrational Modes — No Structural Damage	55
Table 6. First Six Uncoupled Vibrational Modes — EI-30%, GJ-50% Decreased @ sta. 3,4,5.	56
Table 7. First Six Uncoupled Vibrational Modes — EI-40%, GJ-60% Decreased @ sta. 3,4,5.	57
Table 8. First Six Uncoupled Vibrational Modes — EI-50%, GJ-70% Decreased @ sta. 3,4,5.	58
Table 9. First Six Uncoupled Vibrational Modes — EI-30%, GJ-50% Decreased @ sta. 4,5,6.	59
Table 10. First Six Uncoupled Vibrational Modes — EI-40%, GJ-60% Decreased @ sta. 4,5,6.	60
Table 11. First Six Uncoupled Vibrational Modes — EI-50%, GJ-70% Decreased @ sta. 4,5,6.	61
Table 12. First Six Uncoupled Vibrational Modes — EI-30%, GJ-50% Decreased @ sta. 5,6.	62
Table 13. First Six Uncoupled Vibrational Modes — EI-40%, GJ-60% Decreased @ sta. 5,6.	63
Table 14. First Six Uncoupled Vibrational Modes — EI-50%, GJ-70% Decreased @ sta. 5,6.	64

LIST OF TABLES (continued):

	Page
Table 15. Critical Speeds for Damaged Wing — Aerodynamic Site At 60% Semi-Span	65
Table 16. Critical Speeds for Damaged Wing — Aerodynamic Site At 80% Semi-Span	67
Table 17. Critical Speeds for Damaged Wing — Aerodynamic Site At 90% Semi-Span	70
Table 18. First Six Coupled Vibrational Modes — No Structural Damage	75
Table 19. First Six Coupled Vibrational Modes — EI-30%, GJ-50% Decreased @ sta. 5,6	76
Table 20. First Six Coupled Vibrational Modes — EI-40%, GJ-60% Decreased @ sta. 5,6	79
Table 21. First Six Coupled Vibrational Modes — EI-50%, GJ-70% Decreased @ sta. 5,6	82
Table 22. The Influence of Coupled and Uncoupled Vibrational Modes Used on Critical Speed for Aerodynamic Site At 90% Semi-Span With 0° Sweep	85

LIST OF FIGURES

	Page
Figure 1. Aeroelastic Modeling Employing an Elastic Axis Beam-Type Structure and a Strip Theory Aerodynamic Approximation	35
Figure 2. Idealized Aerodynamic Damage Model	36
Figure 3. Drag Divergence Mathematical Model	37
Figure 4. Conservative and Upper Bound Estimates on the Damage-Induced Drag Coefficient C_D^* for Various Maneuvering Load Factors and Combat Altitudes	38
Figure 5. Damage-Induced Drag Force for Various Size Damage Areas and Altitudes for a True Maneuvering Speed of 600 MPH	39
Figure 6. Influence of Spanwise Location of Aerodynamic Damage Site (No Structural Damage) on Drag Divergence and Flutter	40
Figure 7. Influence of Spanwise Location of Aerodynamic and Structural Damage Site on Drag Divergence and Flutter	41
Figure 8. Influence of Wing Sweep on Damage-Induced Drag Divergence	42

LIST OF FIGURES (Continued):

	Page
Figure 9. Influence of Wing Sweep on Damage-Induced Drag Divergence (Aerodynamic Damage at 90% Semi-Span)	43
Figure 10. Proposed Damage Classes	44
Figure 11. Influence of Multiple Damage Site Drag Effects on Flutter and Divergence of Four Swept Wing Configurations	45
Figure 12. A-10 Drag Divergence Damage Model	46
Figure 13. A-10 Mode Shapes and Frequencies Employed in the Drag Divergence Modeling	47
Figure 14. Potential Parametric Instabilities Associated with Damage to Statistical Fighter Wing	48
Figure 15. Summary of Parametric Type Flutter Instabilities Promoted by Periodic, Time Dependent, Damage Induced Drag Forces	49

1. INTRODUCTION

The influence of ballistic damage on the aeroelastic response of an aircraft in flight is not yet well understood. The primary damages of interest are those sustained by the lifting surfaces, that is, the aircraft wings and tail sections. A review of inflight films illustrating ballistic damage to aircraft indicates that in some cases an aircraft can tolerate a significant amount of damage from several hits while in other cases a single hit may result in the immediate destruction of the aircraft. A question naturally arises as to whether a reasonably small amount of damage might occur in a critical area that could promote an explosive type of flutter or divergence instability. These instabilities would most likely destroy the aircraft. In the present study an investigation is carried out to determine whether ballistic damage can seriously degrade the aeroelastic integrity of lifting surfaces on aircraft.

Some of the first and most comprehensive work on this general subject was conducted in 1950 by Biot and Arnold as out-lined in Reference 1. The results of their studies demonstrated that aeroelastic instabilities were not easily triggered by ballistic damage. Furthermore, if sufficient structural damage was imposed on a lifting surface to lower its flutter and divergence speeds into the flight envelope, the surfaces would fail due to inadequate strength rather than due to inadequate stiffness. In essence, the reduction of flutter and/or divergence margins by 25% required nearly an 90% loss of torsional stiff-

ness at a certain critical section within the wing. It was probably the impact of this finding that delayed any further investigation of this subject for nearly 30 years.

A recent investigation by Hemmig, Venkayya, and Eastep (Reference 2) has incorporated more contemporary finite element techniques to model structural damage to lifting surfaces. Their results also suggest the difficulty of reducing flutter and divergence margins of highly redundant lifting surface structures much below the levels suggested by Biot and Arnold. Some further insight into the problem is obtained here, however, when it is demonstrated that highly optimized structural designs may demonstrate increased aeroelastic sensitivity to ballistic damage.

Recent aeroelastic investigations of lifting surfaces within the literature suggests that refinements in the aerodynamic modeling may be in order (3,4). In essence, the chordwise forces due to drag and leading edge suction are found to have an observable influence on the flutter and divergence boundaries for certain wing geometries. In addition, other aerodynamic investigations outlined in References 5 and 6 suggest that wings with a highly optimized aerodynamic configuration may demonstrate increased sensitivity to ballistic damage through larger drag rises. In view of this, the present study concentrates on an extension of the earlier Biot and Arnold work by incorporating into their analysis chordwise forces due to drag that arise as the result of the ballistic damage.

A potential aeroelastic failure mechanism was identified in the first year's study that results from the localized drag that can be generated on a lifting surface due to significant damage to its aerodynamic shape. When this localized drag occurs at critical positions

over the surface, it drastically lowers the divergence speed of the surface. For this reason, this failure mechanism will be referred to as a "drag divergence" mode of instability. The present study extends this drag divergence investigation to a larger range of parameters. This includes several damage site locations to assess the possible trade-offs between the influence of both structural and aerodynamic damage locations on the wing's divergence characteristics.

A second study is made to determine the influence of ballistic damage on more contemporary swept wing configurations. Both swept back and swept forward wings are considered that have the same stiffness distribution along the elastic axis as the statistical straight wing model studied earlier.

The previous drag divergence studies were also extended to allow for the possibility of distributed drag effects and for multiple concentration drag influences on both straight and swept wings. This extension allows, for example, the inclusion of the distributed undamaged wing drag, store drag, gun cannon recoil, and multiple damage site modeling in the aeroelastic analysis.

A second aeroelastic failure mechanism is identified for the case when the damage gives rise to periodic aerodynamic forces in the chordwise plane of the lifting surface. When these periodic forces are appropriately tuned to the structural mode frequencies they can force the wing into a dynamically unstable oscillation known as parametric resonance. This mode of instability is demonstrated on a statistical model of a fighter wing.

Finally, it should be mentioned that the transient structural responses of the lifting surfaces to the pressure forces arising from

the explosive impact of the ballistic warhead are not considered in the present drag divergence study. In essence, only those structural responses are investigated that are due to the steady state or periodic air loads imposed by the damage and the assumed harmonic unsteady or quasi-steady air loads that are classically imposed in a standard flutter analysis.

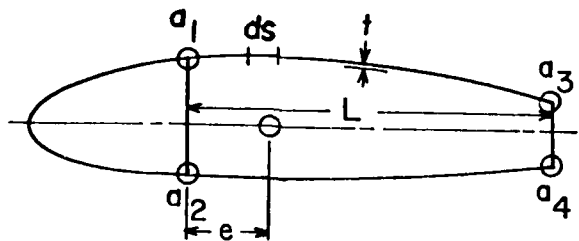
2. DAMAGE IDENTIFICATION

Two types of aircraft lifting surface damage are considered in this report. One is the structural damage which is reflected as a reduction of the bending stiffness (EI) and torsional stiffness (GJ) of the lifting surfaces. The other is aerodynamic damage which is the modification of the aerodynamic forces arising from the change of shape of the aircraft lifting surfaces.

2.1 Structural Damage Modelling

In developing a model for structural damage studies, reference at this point is made to the comprehensive work by Biot and Arnold (Reference 1), which assesses the changes in the physical parameters of a wing, such as rigidity changes, and their secondary effect on inertia due to a shift in elastic axis that might be caused by ballistic damage. In that study, the authors conduct an investigation which involves the flutter analysis of a typical model of a fighter wing subject to a wide range of structural damage conditions. The basic aeroelastic parameters of this typical wing are chosen to be the geometric mean of some fourteen different fighter aircraft. These are representative of early 1950 fighter configurations which have moderate aspect ratio straight wings. It was further demonstrated in this study by Biot that the statistical model reflected the correct trends in modification of aeroelastic characteristics due to damage that was determined for a randomly selected fighter from the group. Table 1 contains a listing of these fourteen aircraft. The geometric mean of the aeroelastic

parameters of this typical model are given in Table 2. Since aircraft of this type are normally designed to withstand loads up to 1.5 times the maximum limit load (load factor 8.0 to 8.67), the structure should normally experience decreases in torsion rigidity (GJ) and bending stiffness (EI) of up to 45% and not undergo strength failure at its limit load factor. Higher percentage could, of course, be tolerated at lower load factor. To model in detail the changes in structural parameters due to damage the two spar wing is idealized as illustrated below.



In the analysis of such a two spar wing it is common practice to neglect all of the material aft of the rear spar where the controls are generally located. A parametric study is conducted on such a model in Reference 1 to determine the shift that could be imposed on the wing elastic axis by ballistic damage. Such a modeling indicates, for example, that even extreme damage patterns result in a movement of the elastic center of the wing by only 12.5% of

the section semi-chord. In essence, it is found that shifts in the elastic axis due to ballistic damage, which still left the structure with adequate strength, would not significantly influence the flutter and divergence margins. Consequently, in the structural damage model employed for the present study only reductions of EI and GJ are applied in the damage area to reflect ballistic damage to the structure. Since the wing structure of this typical fighter is a two spar semi-monocoque construction (see Figure 1), torque box destruction and GJ reduction would probably be easier to accomplish than reducing EI by removing spar cap material. For this reason, the more representative structural damage cases are thought to be those involving larger GJ reduction than EI reductions.

It is apparent that the finite element method can be employed in a more detailed structural modelling when a smaller aspect ratio wing must be identified or when more structural detail is available for a statistical model. The reader is referred to Appendix C and Reference 2 for more information on this type of modelling.

2.2 Aerodynamic Damage Modelling

The present investigation employs basically the same strip theory aerodynamic modelling as utilized in Reference 1. However, one additional parameter (not in Reference 1) is included in this study. This parameter accounts for the steady state chordwise concentrated drag force that occurs as a result of aerodynamic damage. The influence of possible time dependent unsteady drag effects are discussed in Section 7 of this report. This first order influence of the aerodynamic damage is based upon an assumed localized hole through the lifting surface.

Furthermore, this damage is considered to introduce only local or concentrated changes in the aerodynamic lift, drag and moment distributions, as illustrated in Figure 2. This localized modelling of the loads induced by the thru hole type damage is justified based upon the findings from a kernel function lifting surface theory study of these types of discontinuities (Reference 7). Figure 3 illustrates such an example taken from a theoretical study in Reference 7 where a thru hole type damage, shaded region, produces chordwise and spanwise pressure disturbances that die out within a characteristic hole dimension. The experimental observations in Volume II of this report also confirm these findings. A coupling of these damaged induced loads with the thin beam lateral buckling equations for the wing structure results in only the drag providing the first order aeroelastic effect of the damage. It was anticipated that this concentrated type of aerodynamic drag force might be capable of producing a structural failure of the wing even in the absence of significant structural damage. This is illustrated in Figure 4 which indicates that high chordwise drag loads generated near the tip of the wing may cause the wing to snap or diverge laterally similar to the lateral buckling of a thin beam.

An estimate of potential damage-induced drag levels can be obtained from the experimental studies of Reference 8 or 9, where changes due to damage in the lifting surface drag polar

$$C_D = C_{D_{\pi}} + p C_L^2$$

are expressed as changes in the parasite drag coefficient $C_{D_{\pi}}$ and the slope p of the induced drag term. A coefficient of drag

increase C_D^* is defined in terms of a damage area as

$$C_D^* = \frac{\Delta D}{qA} = \Delta C_D \frac{S}{A}$$

S = wing area

A = hole or damage area

and then

$$C_D^* = C_{D_\pi}^* + p^* C_L^2$$

with

$$C_{D_\pi}^* = C_{D_\pi} \frac{S}{A}$$

$$p^* = \Delta p \frac{S}{A}$$

That is, $C_{D_\pi}^*$ and p^* represent increments in the drag polar based upon the hole damage area, i.e., the sum of the entrance and exit hole areas divided by two. A tabulation of experimentally determined values of $C_{D_\pi}^*$ and p^* is given in Table 3. These parameters are measured on a 2-ft. chord and an $8\frac{1}{2}$ -ft. span two-dimensional wing section having a symmetrical NACA 65₁-012 profile. The Reynolds number of the tests is 3.7×10^6 which is sufficiently large that the measurements may be applied to full-scale damaged aircraft. The classes of damage (i.e., leading edge, midchord, etc.) are also presented in Table 3. From this table it is evident that

$$C_{D_\pi}^* \leq 3.4$$

$$p^* \leq 16$$

represent experimentally determined upper bound values for the drag parameters. These larger values occur for the leading edge

class A or B type damage. Based upon the data of Table 3, a conservative damage-induced drag estimate would be

$$C_D^* = 1.0 + 5C_L^2$$

while an upper bound estimate for the higher Mach numbers and larger hole sizes would appear to be

$$C_D^* = 2.4 + 10C_L^2 .$$

These damaged-induced drag coefficients are based upon the assumption that leading edge type damages are imposed upon the lifting surfaces.

To obtain an estimate of the actual levels of damage-induced drag force that can be imposed on the typical fighter aircraft in combat, consider the following fighter parameters.

weight $w = 21,000$ lb (including stores)
wing area $S = 300$ ft 2 (including fuselage carry thru)
aspect ratio = 4.5
 $C_{D_{\pi}} = 0.014$ (clean fighter)
 $C_{D_{\pi}} = 0.026$ (fighter with external stores)
 $p = 0.083$
combat altitude 20,000 ft

Based upon these parameters, an assumed 600 mph flight speed, and the experiments of Reference 9, one can estimate the range of drag increments that would be expected for a range of load factor 'n' and damaged area 'A' expressed in terms of % wing area for several combat altitudes. These results are presented in Table 4 for 20,000 ft altitude and in Figures 5 and 6 for the different combat altitudes.

Several other drag factors that are not considered here could also be simultaneously degrading the divergence characteristics of the wing. External stores on the wing, for example, give rise to concentrated drag and chordwise loadings as does the recoil from firing wing mounted gun systems. The drag on fighters loaded with external stores can be nearly double the drag of a clean fighter in a cruise condition. In addition, the recoil loads on a wing due to rapid gun fire can be on the order of 6000 lbs. to 8000 lbs. Finally, the nearly uniform undamaged wing drag and any induced drag due to aileron control deflection needed to trim the aircraft after damage will also be degrading the divergence characteristics of the wing. Possible combinations of these above factors adding to the damaged induced drag forces can give rise to a degradation of the divergence speed of the statistical fighter wing to within the flight envelope.

A further consideration of the evaluation of damage-induced drag modeling can be found in appendix A.

3. DAMAGE INFLUENCE ON FLUTTER AND DIVERGENCE SPEEDS OF A ZERO SWEEP STATISTICAL FIGHTER WING

A flutter and divergence analysis to investigate the damage influence on the statistical fighter wing is conducted at sea level conditions for a range of aerodynamic damage expressed in terms of damage-induced drag levels. During the studies, three aerodynamic aerodynamic damage configurations are considered. In one case, aerodynamic damage is assumed localized at the 80% semi-span of the wing, while in the second case this damage is moved to 90% semi-span position. Finally, a third case of 60% semi-span location is considered to estimate the tradeoff between aerodynamic and structural damage location.

For a cantilever thin wing with concentrated aerodynamic drag force, the basic mathematical model employs the following classical thin beam coupled bending and torsional equations similar to those employed in lateral buckling studies of thin beams* (Appendix B):

* $H(x)$ in these equations represent the unit step function and is employed here to more compactly write the beam equations that are valid to the right and left of the concentrated load.

$$\begin{aligned}
 & \frac{\partial^2}{\partial x^2} (EI \frac{\partial^2 \omega}{\partial x^2}) + m \frac{\partial^2 \omega}{\partial t^2} + S_\alpha \frac{\partial^2 \beta}{\partial t^2} \\
 & + \Delta D H(\xi-x) [(\xi-x) \frac{\partial^2 \beta}{\partial x^2} - 2 \frac{\partial \beta}{\partial x}] - L(\omega, \beta; x, t) = 0 \\
 & - \frac{\partial}{\partial x} (GJ_{\text{eff}} \frac{\partial \beta}{\partial x}) + I_\alpha \frac{\partial^2 \beta}{\partial t^2} + S_\alpha \frac{\partial^2 \omega}{\partial t^2} \\
 & + \Delta D H(\xi-x) [(\xi-x) \frac{\partial^2 \omega}{\partial x^2}] - M_{ea}(\omega, \beta; x, t) = 0
 \end{aligned}$$

where

$$\Delta D = C_D^* A q$$

(C_D^* = constant determined from experiment; $A = \frac{1}{2}$ total entrance plus exit hole area)

A Galerkin-type solution of these equations for various levels of damage-induced drag is employed using

$$\begin{aligned}
 \omega &= \omega_0 e^{i\omega t} \\
 \beta &= \beta_0 e^{i\omega t}
 \end{aligned}$$

with

$$\omega_0(x) = \sum_{i=1}^r h_i f_i(x)$$

$$\beta_0(x) = \sum_{i=1}^r \beta_j F_j(x)$$

and h_i, β_j defined as complex with $f_i(x)$, $F_j(x)$ determined from normal vibration modes. Three bending $f_i(x)$ and three torsional modes $F_i(x)$ are used during these studies for different classes of structural damage. These modes are presented in Tables 5 through 14.

The appropriate inertial and time-dependent aerodynamic force terms are also included in the analysis thus allowing a complete dynamic, but steady state stability study. For the preliminary studies, incompressible strip theory is employed for the moderately high aspect ratio wings. Finally, a constant static parasite drag term is considered to be the significant or first order aerodynamic force caused by the damage. These drag estimates are deduced from Table 3 taken from Reference 9.

The results of drag divergence and flutter analyses are presented in Tables 15 through 17 and in Figures 7 and 8. The influence of aerodynamic damage alone is illustrated in Figure 7. This damage is in the form of drag only with 100% structural integrity assumed. A hypothetical wing tip location of aerodynamic damage site (100% semi-span) is also presented in Figure 7. This result is based on extrapolation of the data computed for 60%, 80% and 90% semi-span locations for the aerodynamic sites. The

level of drag is seen to play an important role in the transition from a classical flutter critical instability for the undamaged wing to a critical divergence type of instability for a significantly damaged wing subjected to high drag levels. Interestingly enough, the actual flutter speed increases as a result of the added drag term. This is consistent with other findings in the literature for moderate aspect ratio undamaged wings (3, 4). In the present study, the divergence becomes critical due to the high level of localized drag caused by the damage. The near frequency coalescence, characteristic of classical bending torsional flutter, is eliminated or delayed by the tendency of the first mode frequency branch to approach zero frequency, thereby promoting divergence in the first mode branch prior to the occurrence of flutter in the torsion branch.

In spite of the significant reduction in the critical divergence speeds of the wing due to drag, aerodynamic damage alone is not sufficient to reduce these critical speeds to within the flight envelope of our generic fighter wing for reasonable damage-induced drag levels. Consequently, several structural damage configurations are superimposed upon these aerodynamic damage cases to further degrade the wing's critical speeds. These results are presented in Tables 15 through 17 and in Figure 8. As indicated earlier, the structural damage is imposed by locally reducing the torsional rigidity (CJ) and bending stiffness

(EI). Without aerodynamic drag imposed, the flutter speed is seen to decrease due to the loss of structural stiffness. These results are similar to the findings of Reference 1. For the larger reductions of EI and GJ at stations 3,4,5, the critical flutter speed falls into the flight envelope at low drag level. On the contrary, for the damage at station 5,6 the divergence speed is more critical than the flutter speed at moderate to high damage-induced drag levels. These results show that larger structural damage near the wing root will produce a critical flutter condition while aerodynamic drag rises near the wing tip are more critical to divergence. Further investigations between the aerodynamic damage and structural damage site trade-offs are probably in order to further clarify these features.

From Figure 8, for aerodynamic damage at the 80% semi-span, it is evident that for maneuvering flight one combination of aerodynamic and structural damage equivalent to 5% of the wing area (see Figures 5&6) and producing a 70% reduction in torsional and bending stiffness at stations 4, 5 and 6 would reduce the divergence speed of the fighter to approximately 600 mph or to within its flight envelope. Another damage alternative occurs for an aerodynamic damage at 90% semi-span and a resulting 70% reduction in torsional stiffness at stations 5 and 6 with only 50% reduction in bending stiffness. In this case, a 42,000 drag load, caused by a 4½% hole under a 5 'g' pullout, will reduce the divergence speed to within flight envelope. Other tradeoffs are also possible, as is evident from

Figure 8. Fighter aircraft wings of the category of our statistical model are probably designed to a load factor of at least 8.00 to 8.67 with a 1.5 margin on strength under these conditions. In a 5 'g' pull-out maneuver, therefore, our fighter should have adequate strength even though its EI and GJ have been reduced by 60% to 70% in the outer wing panels (10).

4. DAMAGE INFLUENCE ON THE FLUTTER AND DIVERGENCE OF SWEPT WINGS

The influence of ballistic damage on the flutter and divergence characteristics of swept wings is also investigated in the present program. The study employs the elastic axis stiffness distribution of the statistical fighter wing. The equations of motion referenced to the elastic axis can be re-written as

$$\begin{aligned}
 & \frac{\partial^2}{\partial x^2} [EI \frac{\partial^2 \omega}{\partial x^2}] + m \frac{\partial^2 \omega}{\partial t^2} + S_\alpha \frac{\partial^2 \omega}{\partial t^2} \\
 & + \Delta D \cos \Lambda H(\xi-x) [(\xi-x) \frac{\partial^2 \beta}{\partial x^2} - 2 \frac{\partial \beta}{\partial x}] \\
 & - \Delta D \sin \Lambda H(\xi-x) [\frac{\partial^2 \beta}{\partial x^2} + \eta \frac{\partial^2 \beta}{\partial x^2}] - L(\omega, \beta; x, t, \Lambda) = 0 \\
 & - \frac{\partial}{\partial x} [GJ_{\text{eff}} \frac{\partial \beta}{\partial x}] + I_\alpha \frac{\partial^2 \beta}{\partial t^2} + S_\alpha \frac{\partial^2 \omega}{\partial t^2} \\
 & + \Delta D \cos \Lambda H(\xi-x) [(\xi-x) \frac{\partial^2 \omega}{\partial x^2}] \\
 & - \Delta D \sin \Lambda H(\xi-x) [\eta \frac{\partial^2 \omega}{\partial x^2}] - M(\omega, \beta; x, t, \Lambda) = 0
 \end{aligned}$$

where Λ is the angle of swept back of the elastic axis and η is chordwise location of the damage-induced drag.

Due to the large range of wing sweep considered, the interaction between bending and twisting deformations greatly affects the modes and frequencies of vibration. An uncoupled bending and torsional mode vibration analysis is no longer valid for generating assumed modes to be employed in a Galerkin analysis. Instead of using the uncoupled modes, a Galerkin-type solution of the flutter equations is written as:

$$\omega = \sum_{i=1}^r h_i(x) g_i(t)$$

$$\beta = \sum_{i=1}^r \beta_i(x) p_i(t)$$

where $g_i(t)$ and $p_i(t)$ are the generalized coordinates and $h_i(x)$ and $\beta_i(x)$ are introduced as the coupled bending and torsional vibration modes. During the swept wing studies, aero-dynamic damage is located at 90% of the semi-span and different structural damage cases are imposed at Stations 5 and 6. The six coupled modes, used for this flutter study, are given in Tables 18 through 21.

The numerical studies in this section are limit checked against the results of Section 3 by considering the special case of zero wing sweep. A comparison of these computed results are illustrated in Table 22. Column 'A' here represents the flutter and divergence results for zero wing sweep taken from Section 3

and Table 17. The results are obtained using uncoupled vibration modes in a Galerkin analysis. Column 'B' is a solution to the same problem taken from the studies of the present section employing coupled vibration modes in a Galerkin-type solution of the flutter equations. The divergence speeds are seen to agree within 1% while differences in computed flutter speeds are less than 5%.

Wing sweep backs of 20° and 40° are investigated for a 90% semi-span damage site location while a swept forward wing of -20° is also checked as a reference configuration. The result of the study for aerodynamic damage only with $n = 0$ is illustrated in Figure 9a normalized against the divergence speed of the respective swept wing for no aerodynamic damage. A review of Figure 9a suggests that a critical wing sweep exists in the neighborhood of 20° that is most susceptible to aerodynamic damage. The influence of two chordwise locations of the aerodynamic damage site is considered for a sweep of $+20^{\circ}$. One site is chosen forward of the elastic axis 0.833 ft ($n < 0$) and one aft of the elastic axis by 0.833 ft ($n > 0$). This change of chordwise damage site location is found to produce less than a 2% difference in the flutter and divergence speeds between the two cases. Aerodynamic damage induced forward of the elastic axis appears to be slightly more destabilizing. The influence of a combined aerodynamic and structural damage investigation is also illustrated in

Figures 9b, c & d. The results demonstrate that structural damage degrades the flutter and divergence characteristics of swept-back wings to a much greater extent than for unswept wings. The larger the sweep-back, the larger the reduction in divergence speeds that occur. The very low divergence speeds associated with the swept-forward wing are also illustrated here. The apparent lesser influence of the structural damage on swept-forward wings is most likely due to the already inherently low divergence speeds associated with these configurations. The results of the trade-off study in spanwise damage site location indicates flutter again may be the crucial instability for ballistic damage near the wing root, while drag divergence becomes the crucial instability for damage near the wing tip.

5. INFLUENCE OF DISTRIBUTED AND MULTIPLE DAMAGE SITE DRAG EFFECTS ON FLUTTER AND DIVERGENCE OF STRAIGHT AND SWEPT WINGS

The investigations of Sections 3 and 4 can be generalized to the distributed and multiple concentrated drag effects illustrated in Figure 10. It is to be emphasized, however, that the actual drag levels and spanwise distribution must be determined from wind tunnel tests as no theory will, at present, predict these. Undamaged drag effects can also be included in this generalization. It is based upon the assumption that the distributed loading can be "beamed" or lumped to the nodal points of the structure as is done in any standard finite element or collocation analysis. In the case of a series of finite concentrated damage sites the method becomes exact. The appropriate equations are readily identified as:

$$\begin{aligned}
 & \frac{\partial^2}{\partial x^2} \left[EI \frac{\partial^2 \omega}{\partial x^2} \right] + m \frac{\partial^2 \omega}{\partial t^2} + S_\alpha \frac{\partial^2 \omega}{\partial t^2} \\
 & + \sum_{j=1}^N \Delta D_j \cos \Lambda H(\xi_j - x) \left[(\xi_j - x) \frac{\partial^2 \beta}{\partial x^2} - 2 \frac{\partial \beta}{\partial x} \right] \\
 & - \sum_{j=1}^N \Delta D_j \sin \Lambda H(\xi_j - x) \left[\frac{\partial^2 \beta}{\partial x^2} + n \frac{\partial^2 \beta}{\partial x^2} \right] - L(\omega, \beta; x, t, \Lambda) = 0 \\
 & - \frac{\partial}{\partial x} \left[GJ_{\text{eff}} \frac{\partial \beta}{\partial x} \right] + I_\alpha \frac{\partial^2 \beta}{\partial x^2} + S_\alpha \frac{\partial^2 \omega}{\partial t^2} \\
 & - \sum_{j=1}^N \Delta D_j \sin \Lambda H(\xi_j - x) \left[n \frac{\partial^2 \omega}{\partial x^2} \right] - M(\omega, \beta; x, t, \Lambda) = 0
 \end{aligned}$$

where j is an integer and N is the number of concentrated drag sites or nodal points used in discretizing the distributed drag loading. The other parameters are identified in Section 4.

To illustrate the influence of distributed drag modeling on wing flutter and divergence speeds a multiple or distributed damage case was investigated numerically. The results of this study are illustrated in Figure 11 for four cases of wing sweep. The centroid of the loading system is also identified in these figures. Drag levels at Stations 5 and 6 were taken to be double those at Station 4 for this damage configuration. Structural damage, when imposed, was considered occurring only at Stations 5 and 6. By comparing the results of Figure 11a (zero sweep case) with the data of Figure 8 for damage at 80% semi-span, it is evident that the general trends of flutter and divergence boundaries with drag level are similar for distributed and concentrated drag loadings. A further review of these figures for no structural damage indicates, however, that replacing the distributed load by its geometric equivalent concentrated load, acting at the centroid of the distributed drag force, predicts too low a flutter and divergence speed estimates for this case. The estimate is approximately 20% lower than it should be for divergence speed predictions. This is most likely due to the fact that the drag is actually distributed over 1/3 of the semi-span and does not closely approximate a concentrated loading such as for the localized thru hole case. Reviewing the other sweep cases indicates as before that structural damage has a more pronounced influence on swept back configurations than on swept forward or on wings with zero sweep.

It was again found for the distributed drag cases that as the damaged induced drag level increased, the flutter speed also increased for all levels of imposed structural damage. This was also found to be the case for the concentrated drag configurations. In addition, wing divergence speeds, as in the concentrated drag case, always decreased with increasing damage induced drag levels.

In many failure cases an aeroelastic collapse of a damaged wing may result as the action of several drag factors. As an illustration, in the above example ΔD_4 could arise from external store drag or from the recoil of a rapid firing cannon mounted in the wing. The damaged induced wing drag at the outer tip might then be represented by ΔD_5 and ΔD_6 . The recoil from a 20 min. rapid firing cannon mounted on the wing might be on the order of 4,000 to 8,000 pounds. For the above simple illustration this would produce total chordwise loadings on the wing on the order of 20,000 to 40,000 pounds. A review of figures 5 and 6 for sea level 600 mph flight condition indicate that such damage induced drag levels of 16,000 and 32,000 pounds respectively can be attributed to low load factor flight conditions. It is evident from this study that distributed drag effects allow for a combined interaction of several factors which may require an extensive parameter tradeoff or optimization study to pin down the extreme cases of interest. The above illustration merely demonstrates how several interacting drag factors can be integrated into the analysis. Drag divergence, even for the case of distributed drag influence, is still considered to be a critical failure mechanism only for high load factor maneuvering flight conditions. Further parameter tradeoff studies, however, are still needed here.

6. COMPARISON OF THE PREVIOUS STRIP THEORY DRAG DIVERGENCE MODELLING WITH A LIFTING SURFACE THEORY MODELLING

The strip theory aerodynamic modelling employed for lifting surfaces investigated in the present and earlier studies is a two-dimensional approximation to a three dimensional surface configuration valid for high aspect ratios. In view of this, an extension of the previous drag divergence studies to lifting surface theory modelling seems necessary to further evaluate the drag divergence failure mechanism on the more moderate aspect ratio fighter wings.

Drag divergence investigations were conducted employing the kernel function lifting surface theory of Cunningham outlined in Reference 19. These studies were conducted on the statistical fighter wing defined in Table 2, and on a modified cantilever model of the A-10 wing illustrated in Figures 12 and 13. The results of the study are presented below and plotted in Figure 9. The imposed aerodynamic damage induced drag is located at the 90% semi-span position. Structural damage was not applied.

Statistical Fighter Wing

Damage Induced Drag Level ~ lbs	Divergence Speed mph	
	Strip Theory	Lifting Surface
0	1450 mph	1334 mph
25,919		880
28,021	915	

Modified A-10 Wing

<u>Damaged Induced Drag</u>	<u>Divergence Speed mph</u>	
<u>Level ~ 1bs</u>	<u>Strip Theory</u>	<u>Lifting Surface</u>
0	890	920
24,467		855
25,509	873	

In all of the above cases the predicted difference in divergence speeds between the two analyses is seen to be less than 9% and in fact less than 5% in nearly all cases studied. The trends in the statistical fighter wing furthermore correctly predict the changes in flutter and divergence properties with damage induced drag that were calculated for the A-10 wing. This should not be surprising since the A-10 wing is similar in design and structure to the statistical fighter wing.

In summary these preliminary studies indicate that incompressible strip theory and the lifting surface theory of Reference 19 are in good agreement when it comes to predicting drag divergence failure of the statistical fighter wing and a modified A-10 wing.

7. SIGNIFICANCE OF DAMAGED INDUCED UNSTEADY DRAG EFFECTS ON PROMOTING FAILURE OF LIFTING SURFACES

It has been shown experimentally in wind tunnel tests that certain classes of damage to a lifting surface can produce high localized mean drag levels. Such high drag levels occur, as shown in the previous sections, under large load factor maneuvering flight conditions and can lead to an aeroelastic failure phenomenon known as drag divergence. A different aeroelastic failure mechanism, however, can also be envisioned even for non-maneuvering flight conditions and much lower drag levels when a periodic time dependent fluctuation occurs in the damage induced drag force. (Figure 14). Such loadings can induce both parametric and combination resonances on a wing structure (References 14, 15, 16, 17, 18).

Parametric instabilities or resonances of structures are well studied in the literature and occur over specific ranges of frequencies of forcing function (fluctuating drag) in the vicinity of

$$\omega \approx 2\omega_n/k \quad k = 1,2,3$$

where the ω_n 's are the characteristic frequencies of the structural system ($n = 1,2,\dots$). For non-conservative systems there is generally a value of pulsating forcing level below which parametric resonance is impossible, irrespective of ω (References 14, 18). So called combination resonance, on the other hand, occurs in the neighborhood of

$$\omega \approx (\omega_n \pm \omega_j) \quad k = 1, 2, \dots$$

with $j \neq n$. Numerical Floquet analysis has been shown to be effective in predicting both parametric and combination resonances (Reference 14).

Figure 14 illustrates the implications of such phenomenon for amplitude levels of time dependent drag loadings ΔD_1 and mean static loadings ΔD_0 that may be much less than the critical drag divergence load ΔD_{cr} . Unstable regions exist, shaded areas, where the wing undergoes dynamic oscillations of increasing amplitude produced by fluctuating drag loads that are appropriately tuned to the wing natural frequencies. The appropriate condition of tuning is roughly given by the above expressions for ω . It is not difficult to envision aerodynamic damage configurations that give rise to periodic forces. For example, the blunted trailing edge of a wing can produce periodic shedding and air loads while an unstable shock configuration induced by damage will also produce oscillatory forces. It should be emphasized, however, that an adequate definition of such time dependent forces can only be obtained from experimental wind tunnel studies on appropriately damaged models.

Generally the nonconservative nature of the structural damping forces and the distributed aerodynamic forces on the wing will preclude the shaded regions from touching the frequency axis. These unstable regions will terminate at some small but finite $\Delta D_1/D_{cr}$.

The system of equations developed in section 5 also govern the time dependent damaged induced drag problem when the drag terms ΔD_j are assumed to be time dependent. Since a significant mean drag term ΔD_0^j may develop due to damage in addition to a fluctuating drag component, the drag ΔD_j is expressed as

$$\Delta D_j = \Delta D_0^j + \Delta D_1^j F(t) , \quad \frac{\Delta D_1^j}{\Delta D_0^j} < 1$$

$$F(t) = F(t + T)$$

T = Period of Motion

where the function $F(t)$ as determined from wind tunnel tests, can be identified in terms of its Fourier components.. The solution of the resulting partial differential equations with variable but periodic coefficients is then reduced to a system of Hill equations thru a Galerkin approximation of the spacial variables as outlined in Section 3. Numerical Floquet analysis can then be effectively employed to solve this system of Hill equations to determine the regions of both parametric and combination resonances illustrated by the shaded regions of Figure 14.

To illustrate the occurrence of this phenomenon, preliminary numerical solutions were obtained for the statistical fighter wing studied earlier in this report. For a drag force fluctuating harmonically with frequency Ω_f , a two mode Galerkin analysis was employed utilizing the first bending and torsion modes of the straight elastic axis fighter wing. The resulting coupled Hill's equations were then solved for small values of $\Delta D_0 / \Delta D_{cr}$ employing the perturbation procedure of Reference 17. Since Hsu's scheme is restricted to only a special class of nonconservative systems the distributed aerodynamic lift and moment where initially excluded and only the time dependent drag terms included in the analysis as the first order fluid effect. The results of the study are illustrated in Figure 15 where the shaded areas indicate the regions of instability. Should the periodic forcing frequency Ω_f of the damaged induced drag force

fall within the shaded regions of the plot the wing structure will become dynamically unstable. That is, its oscillatory motion will increase exponentially with time.

The study for the inclusion of distributed lift and moment as well as for the fluctuating damage induced drag loading must include a transient aerodynamic force modelling. This has been initially approximated by a quasi-steady strip theory for subsonic Mach numbers and a piston theory approximation for supersonic Mach numbers. A classical Galerkin solution is then employed along with an eighth order variable step Runge-Kutta integrator in a numerical Floquet analysis to examine the stability of the damaged wing configuration. These results are currently under development but preliminary studies here are in basic agreement with Figure 15 except near $\Delta D_0 / \Delta D_{cr} \rightarrow 0$ where aerodynamic damping effects eliminate any possible unstable regions.

8. CONCLUSIONS

Aeroelastic failure modes due to warhead damage have been investigated for several lifting surface configurations. The damage model includes both structural and aerodynamic modifications to the lifting surface. Structural damage is reflected as reductions of the stiffness distributions EI and GJ in the region of the damage while aerodynamic damage is included to first order in the form of a drag rise localized at the damage site. Classes of damage producing relatively small steady state drag rises but significant reductions in EI and GJ inboard on the wing degrade the flutter speed of a statistical fighter wing to within its flight envelope. On the other hand, for structural damage in the outer wing panels which produces high steady state drag rise, divergence becomes the critical mode of instability. Under high load factor maneuvers, this divergence speed can drop to within the flight envelope of the aircraft.

The influence of warhead damage on the aeroelastic response of swept wings is carried out over a range of swept back and swept forward planforms. The study indicates that aerodynamic damage in the form of drag rise is the most critical to wings with approximately a 20° swept-back planform. Structural damage also appears more critical to swept back wing configurations. The greater the wing sweep-back, the greater the influence of structural damage in reducing the flutter and divergence speeds of the wing. Additional trade-off studies for damage site locations on swept-back wings are desirable.

The results of the present study are consistent with the findings of Reference 1 when aerodynamic damage is ignored and only structural damage is considered.

An evaluation of the drag divergence modeling employing an incompressible strip theory aerodynamic approximation provided drag divergence boundaries within 5% of those predicted by a more refined lifting surface theory. In the case of the statistical fighter wing the boundaries predicted by strip theory were found to be 3 to 9% higher in velocity than those predicted by lifting surface theory; while for a modified A-10 wing the divergence speeds were approximately 3 to 5% below those estimated by the lifting surface aerodynamic theory. In the summary, the aeroelastic drag divergence modeling employing incompressible strip theory is providing an accurate estimate of the drag divergence features for a damaged wing.

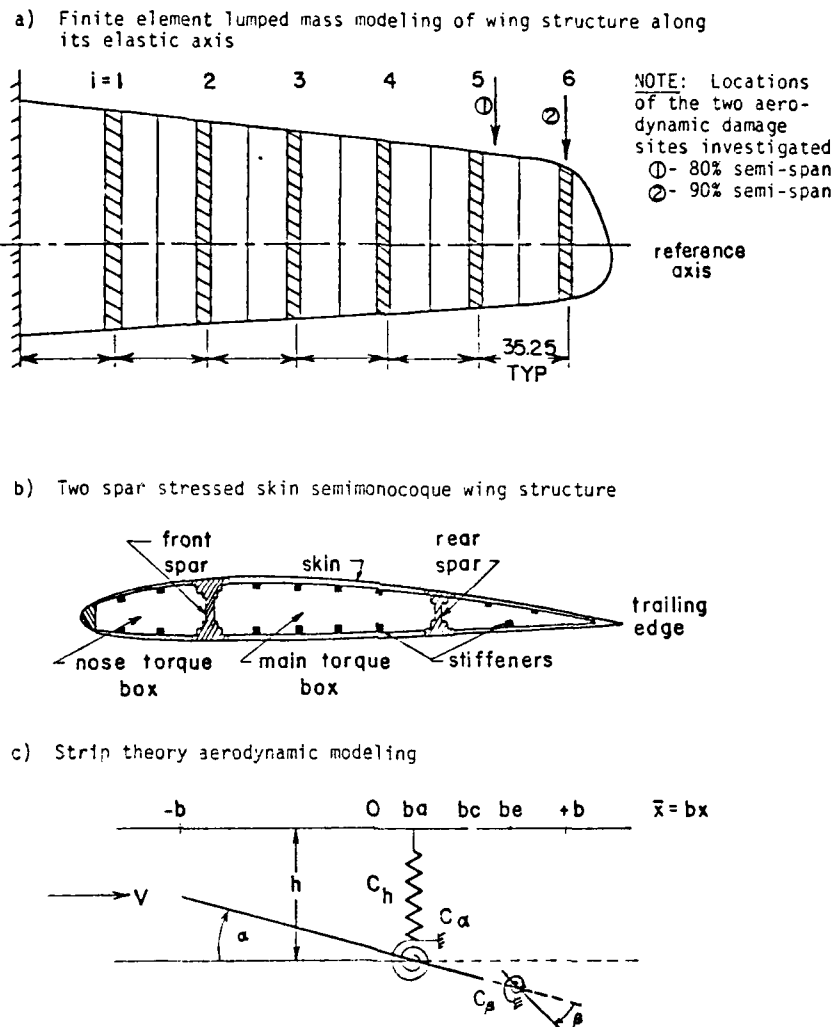
A second aeroelastic failure mechanism can be identified for damaged wings when a periodic chordwise force is generated by the aerodynamic damage. Under these conditions "so called" parametric and combination resonance or instability has been shown to occur when the periodic chordwise force is tuned to the structural resonant frequencies of the wing. The magnitude of the drag forces producing this instability can be much less than those causing drag divergence.

Since the validity of the proposed damage-induced aeroelastic failure mechanism are strongly dependent upon an accurate assessment of aerodynamic damage in the form of damage-induced drag increments, more experimental wind tunnel studies over the results of Reference 11 appear necessary. Finally, further refinements in the aeroelastic modeling are also recommended to allow for the time dependent character of the warhead blast loads.

REFERENCES

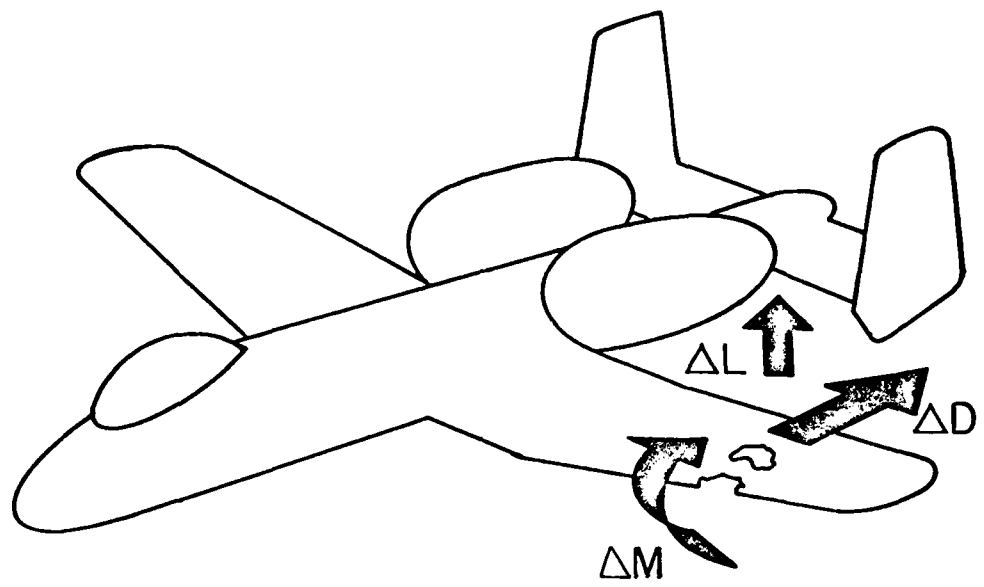
1. Biot, M. A., and Arnold, L., "Study of Vulnerability of Aircraft to Damage-Induced Flutter", Ballistic Research Laboratories Report No. 743, Oct., 1950.
2. Hemmig, F. G., Venkayya, V. B., and Eastep, F. E., "Flutter Speed Degradation of Damaged, Optimized Flight Vehicles", AIAA/ASME/ASCE/AHS 20th Structures, Structural Dynamics, and Materials Conference, St. Louis, Mo., April 4-6, 1979.
3. Petre, A. and Ashley, H., "Drag Effects on Wing Flutter", Journal of Aircraft, Vol. 13, No. 10, Oct., 1976, pp. 755-763.
4. Boyd, W. N., "Effect of Chordwise Forces and Deformations Due to Steady Lift on Wing Flutter", SUDARR No. 508, December, 1977 (AFOSR Contract 74-2712).
5. Henderson, W. P. and Hoffman, J. K., "Effect of Wing Design on the Longitudinal Aerodynamic Characteristics of a Wing-Body Model at Subsonic Speeds", NASA TN D-7099, 1972.
6. Henderson, W. P., "Effect of Wing Leading-Edge Flap Deflection on Subsonic Longitudinal Aerodynamic Characteristics of a Wing-Fuselage Configuration with a 44° Swept Wing", NASA Technical Paper 1351, Nov., 1958.
7. Stearman, R. et. al., "The Influence of Ballistic Damage on the Aeroelastic Characteristics of Lifting Surfaces", AFOSR TR 80-0220, May, 1979.
8. Shatz, R. E., "Aerodynamic Vulnerability of Aircraft", Final Report No. G1-634-G-14, Cornell Aeronautical Laboratory Inc., Mar. 31, 1952.
9. Reece, J. W., "Interpretation of the Drag Changes Measured in the Wind Tunnel Tests of a Holed Wing", Cornell Aeronautical Laboratory, Inc., Report No. G1-634-G-1, Mar., 1952.
10. "Military Specifications--Airplane Strength and Rigidity Flight Loads", MIL-A-8861 (ASG), May 18, 1960 - Table 1, Symmetric Flight Parameters.
11. "Investigations of Characteristics of Airflow within Aircraft Structures--Phase b(1)", Cornell Aeronautical Laboratory, Inc., Report No. V-699-D-17, April, 1952.

12. Abott, Ira H. and von Doenhoff, Albert E., Theory of Wing Sections, Dover, 1959.
13. Sechler, E., Elasticity in Engineering, Wiley Publishers 1952, pp. 369-372.
14. Paidoussis, M.D. and C. Sundararajan, Parametric and Combination Resonances of a Pipe Conveying Pulsating Fluid, Transactions of the ASME, Journal of Applied Mechanics, December 1975.
15. Dungundji, John, Lateral Bending-Torsion Vibrations of a Thin Beam Under Parametric Excitation, AFOSR TR 72-2007, June 1972.
16. Krajcinovic, D.P. and Herrman, G., Parametric Resonance of One-Dimensional Structures Subjected to Periodic Impacts, AFOSR 68-0753, February 1960.
17. Hsu, C.S., On the Parametric Excitation of a Dynamic System Having Multiple Degrees of Freedom, Journal of Applied Mechanics, September 1963, pp. 367-372.
18. Bohn, M.P. and Herrmann, G., The Dynamic Behavior of Articulated Pipes Conveying Fluid with Periodic Flow Rate, Journal of Applied Mechanics, Vol. 41, Transaction ASME, Series E., March 1974, pp. 55-62.
19. Cunningham, A.M. Jr., "A Steady and Oscillatory Kernel Function Method for Interfering Surfaces in Subsonic, Transonic, and Supersonic Flow," NASA CR-144895.
20. Stearman, et. al., "An Investigation of the Influence of Structural Discontinuities on the Performance of Composite Rotor Blades and Panels", AVSCOM Technical Report, Engineering Support Branch, Corpus Christi Army Depot, August 1979.
21. Johnson, C. Philip, "A Frontal-Based Solver with Multi-Level Sub-structuring", ASCE Symposium 1977, Proceedings.
22. Yargicoglu, Atalay I., Johnson, C. Philip, and Stearman, Ronald O., "The Influence of Repair Procedures on the Performance of Composite Rotor Blades", Project Report, Civil Engineering Department, University of Texas at Austin, October 1976.
23. Breihan, J., Kerr, T., and Wendelsdorf, J., "The Correlation of Calculated and Measured Natural Frequencies and Mode Shapes of a Typical Teetering Rotor Blade", Course Report, Aerospace Engineering Department, University of Texas at Austin, May 1978.



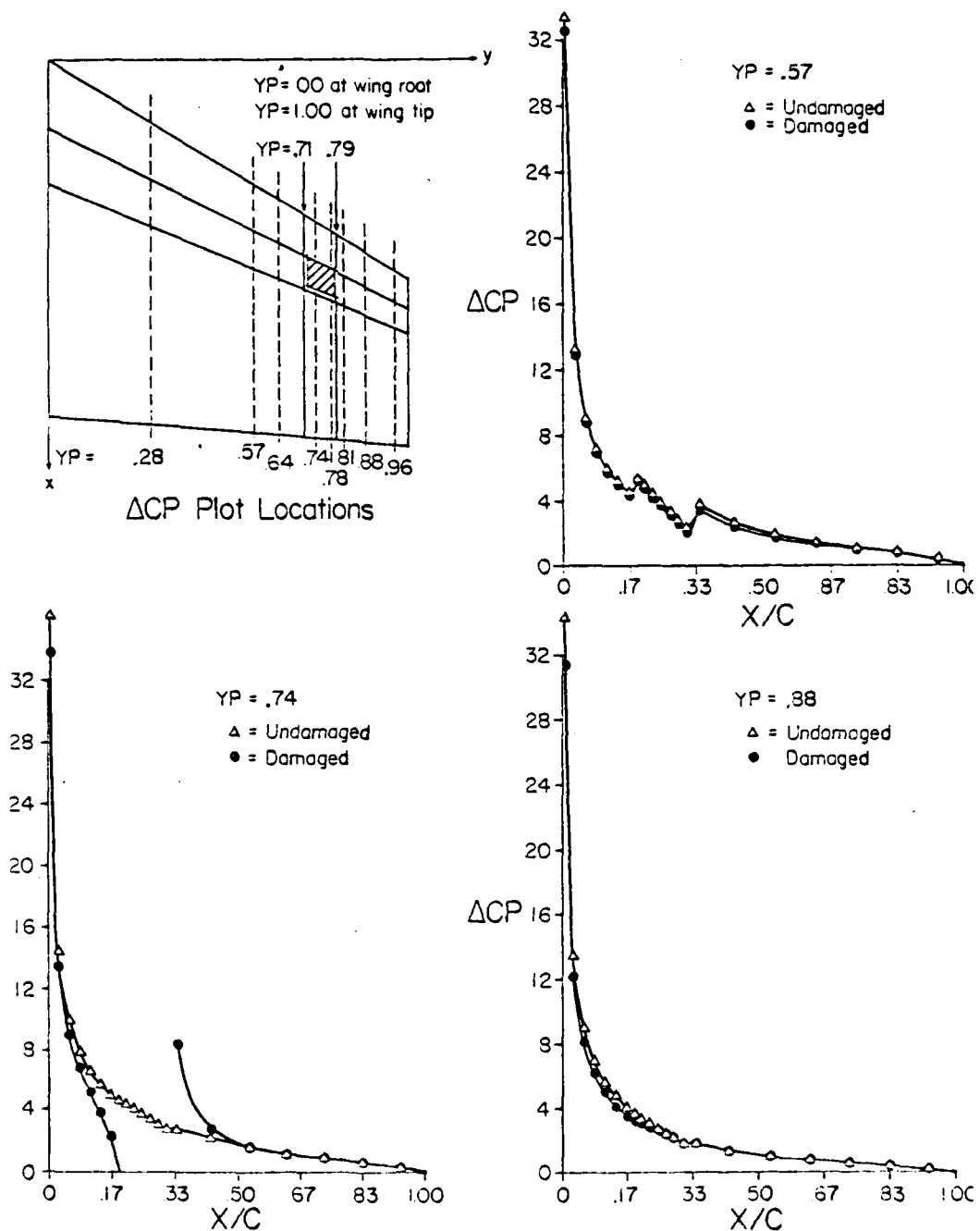
AEROELASTIC MODELING EMPLOYING AN ELASTIC
 AXIS BEAM TYPE STRUCTURE AND A STRIP
 THEORY AERODYNAMIC APPROXIMATION

Figure 1



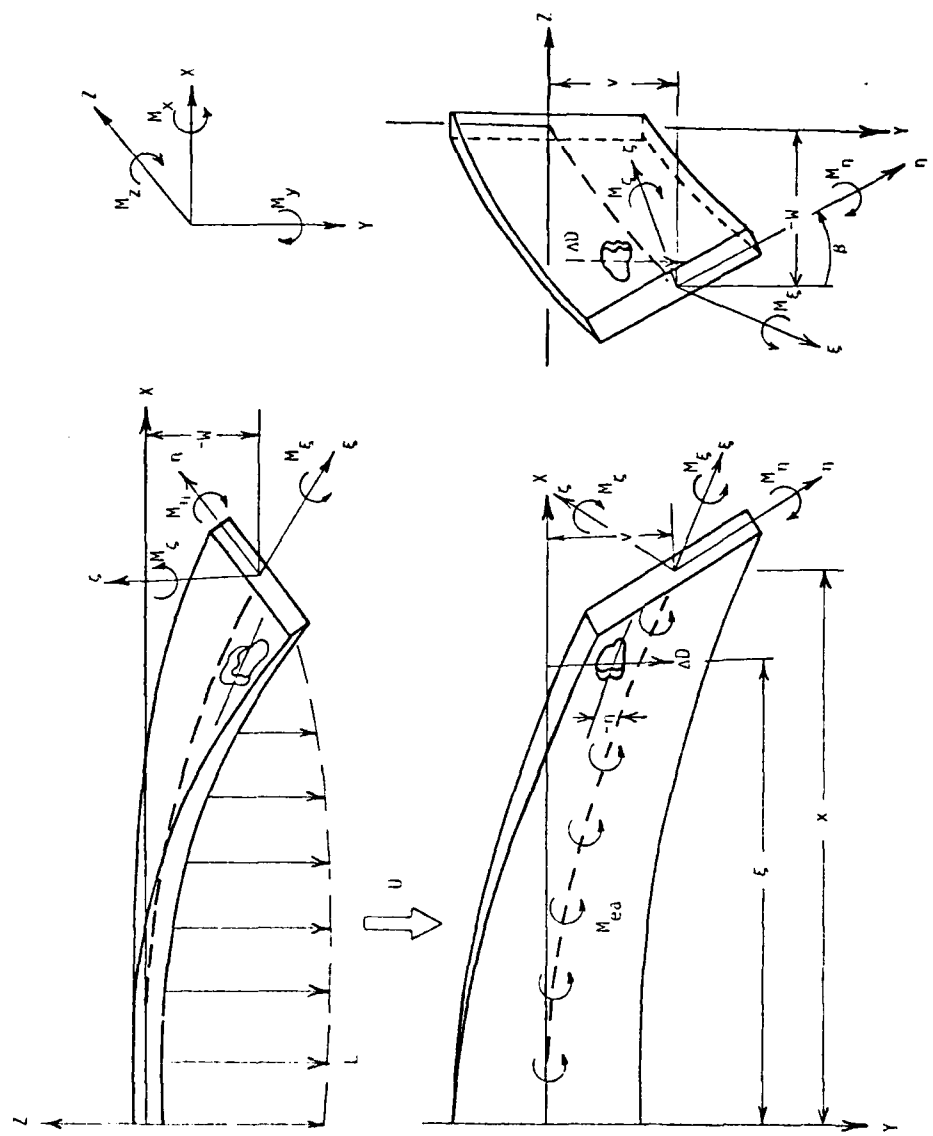
IDEALIZED AERODYNAMIC DAMAGE MODEL

Figure 2

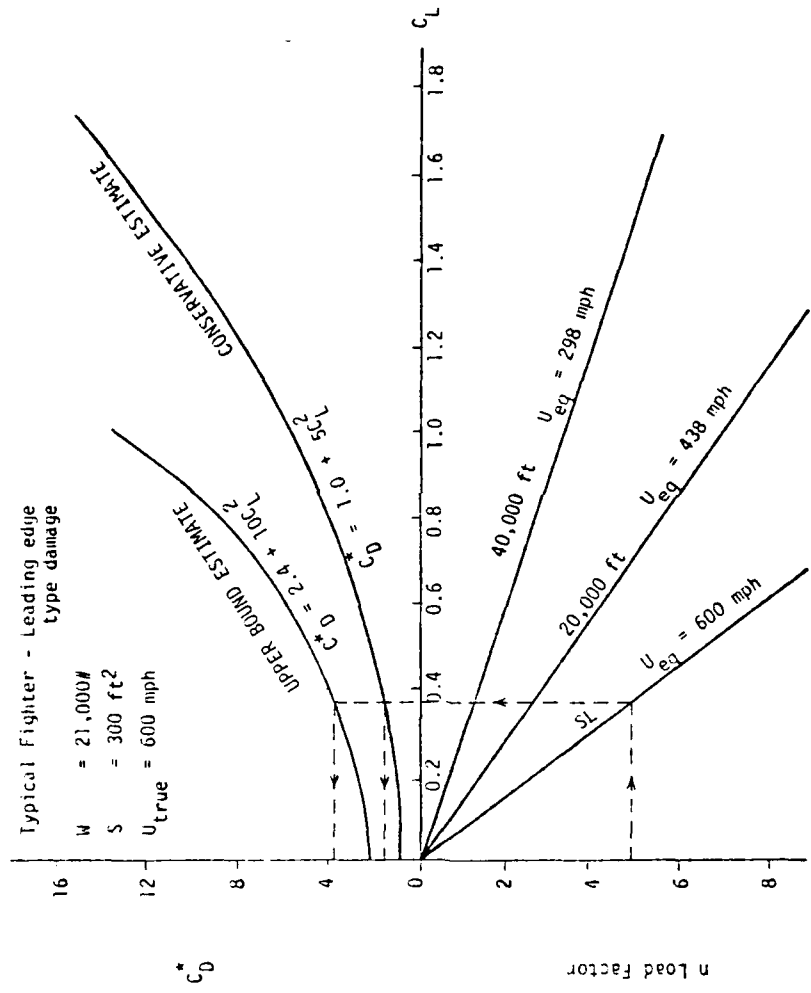


THEORETICALLY PREDICTED PRESSURE DISTURBANCES PRODUCED BY A THRU-HOLE TYPE DAMAGE (SHADeD REGION) ON A MODERATE ASPECT RATIO LIFTING SURFACE WITH TAPER

Figure 3

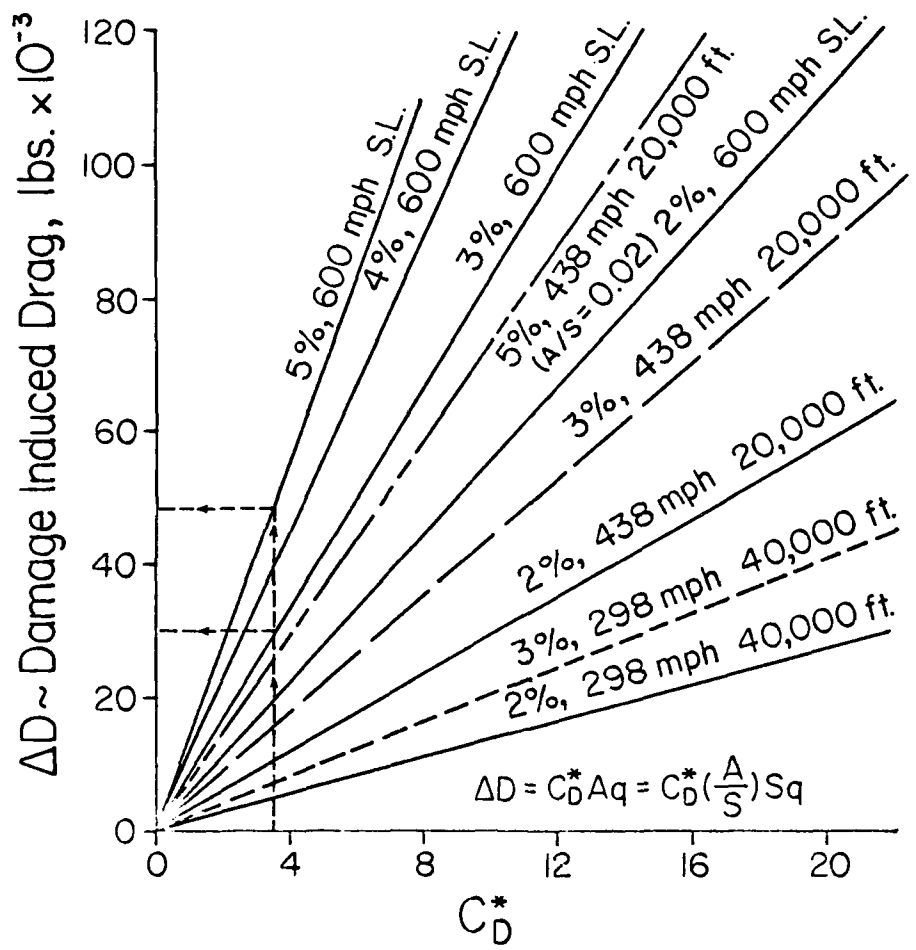


DRAG DIVERGENCE MATHEMATICAL MODEL
Figure 4



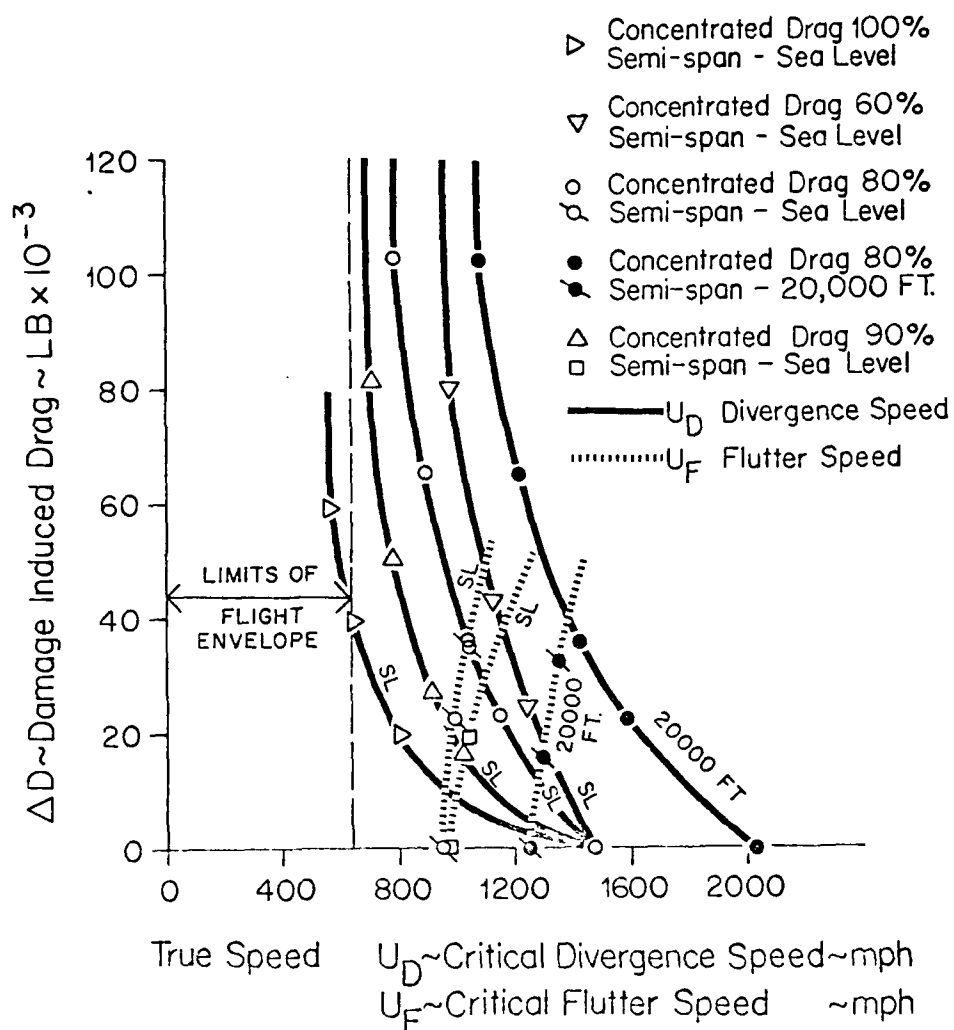
CONSERVATIVE AND UPPER BOUND ESTIMATES ON THE DAMAGED INDUCED DRAG COEFFICIENT C_D^*
FOR VARIOUS MANEUVERING LOAD FACTORS AND COMBAT ALTITUDES

Figure 5



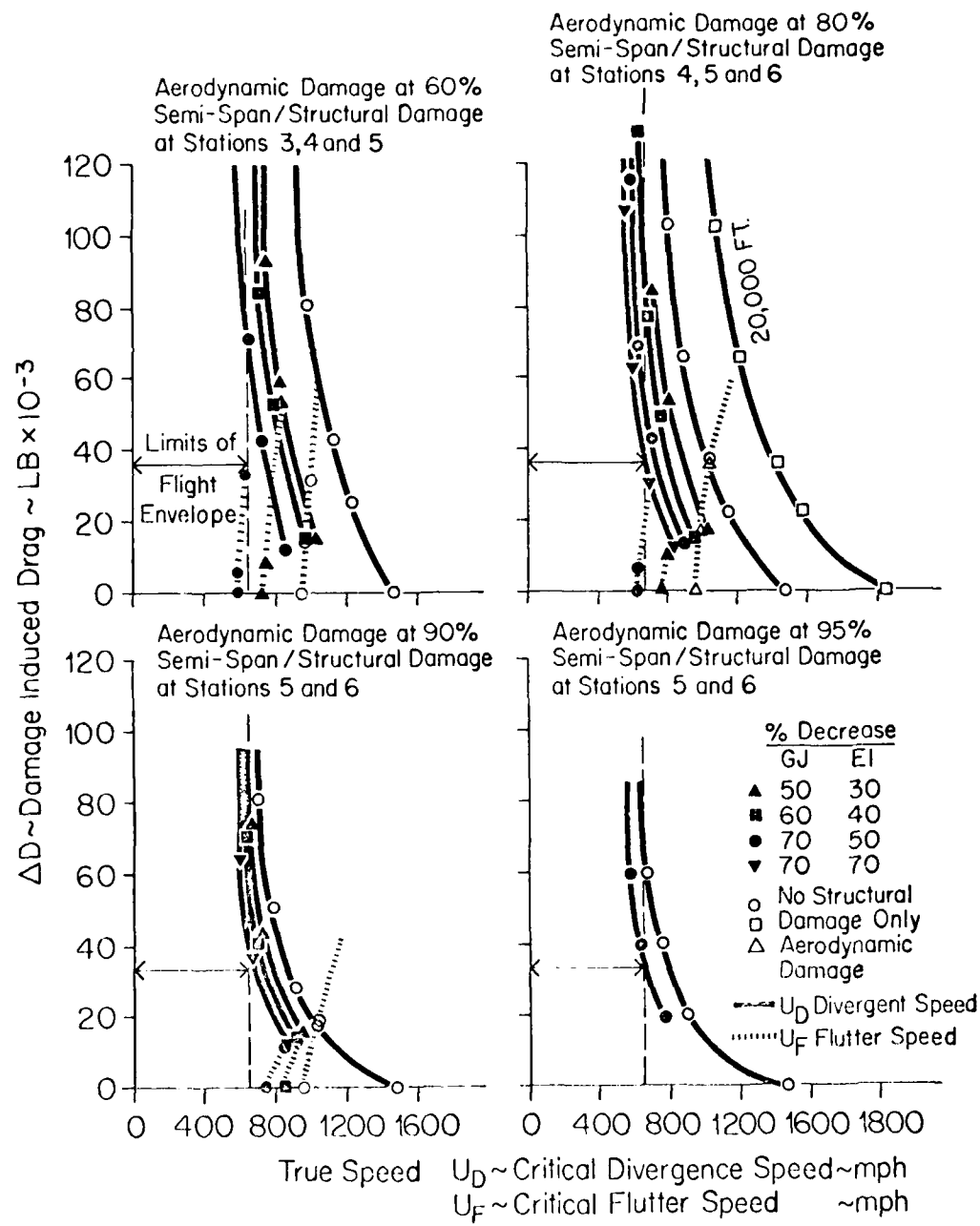
DAMAGE-INDUCED DRAG FORCE FOR VARIOUS SIZE DAMAGE AREAS AND ALTITUDES FOR A TRUE MANEUVERING SPEED OF 600 MPH

Figure 6



INFLUENCE OF SPANWISE LOCATION OF AERODYNAMIC DAMAGE SITE (NO STRUCTURAL DAMAGE) ON DRAG DIVERGENCE AND FLUTTER

Figure 7



INFLUENCE OF SPANWISE LOCATION OF
 AERODYNAMIC AND STRUCTURAL DAMAGE SITE
 ON DRAG DIVERGENCE AND FLUTTER

Figure 8

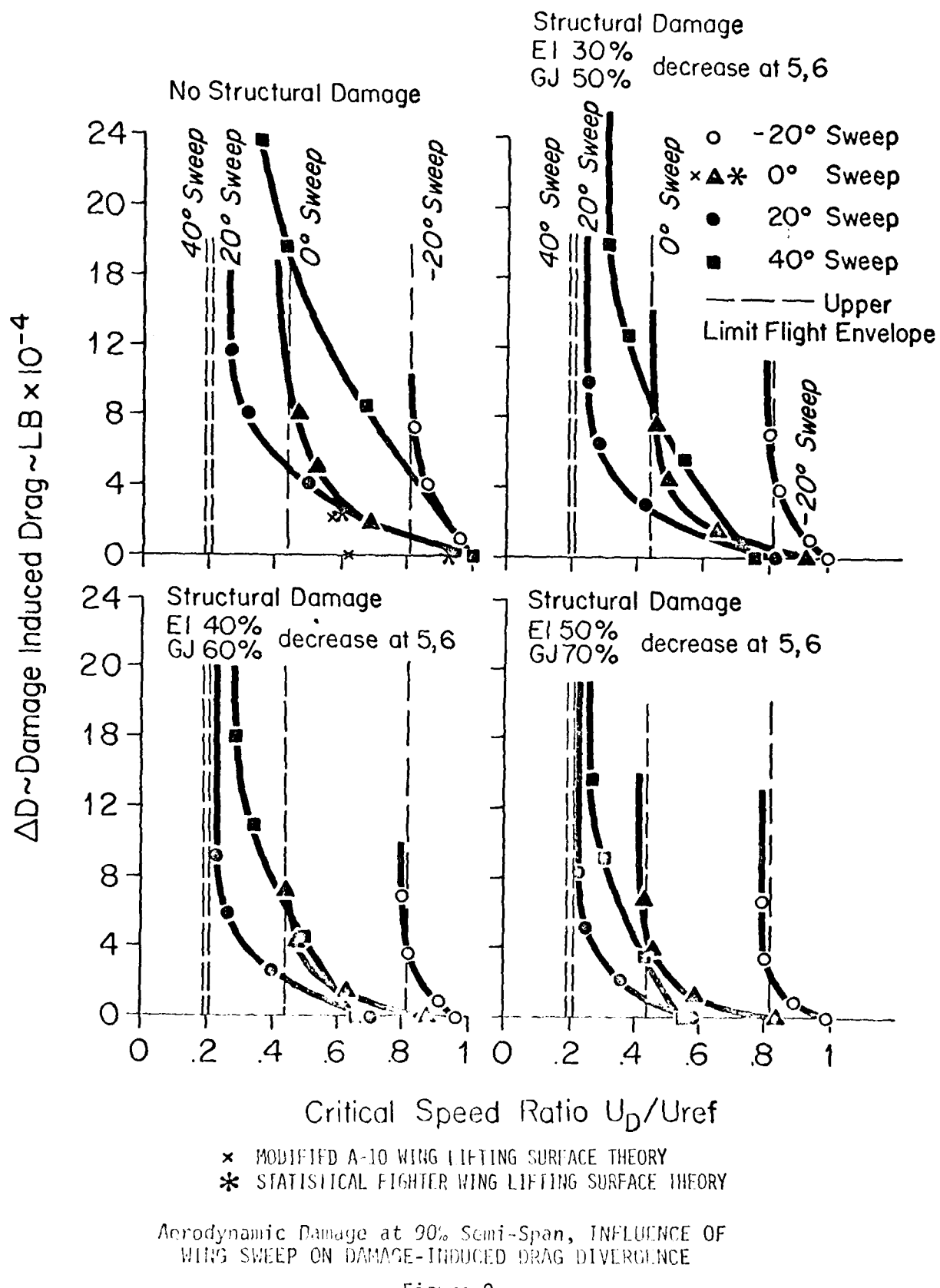
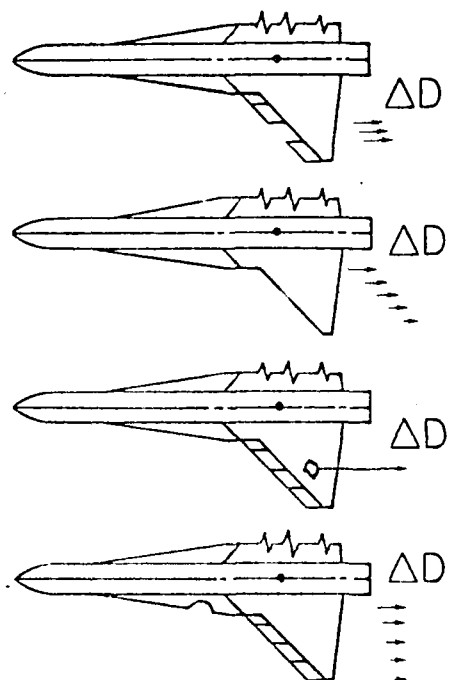
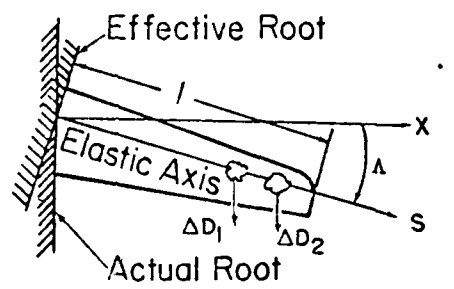
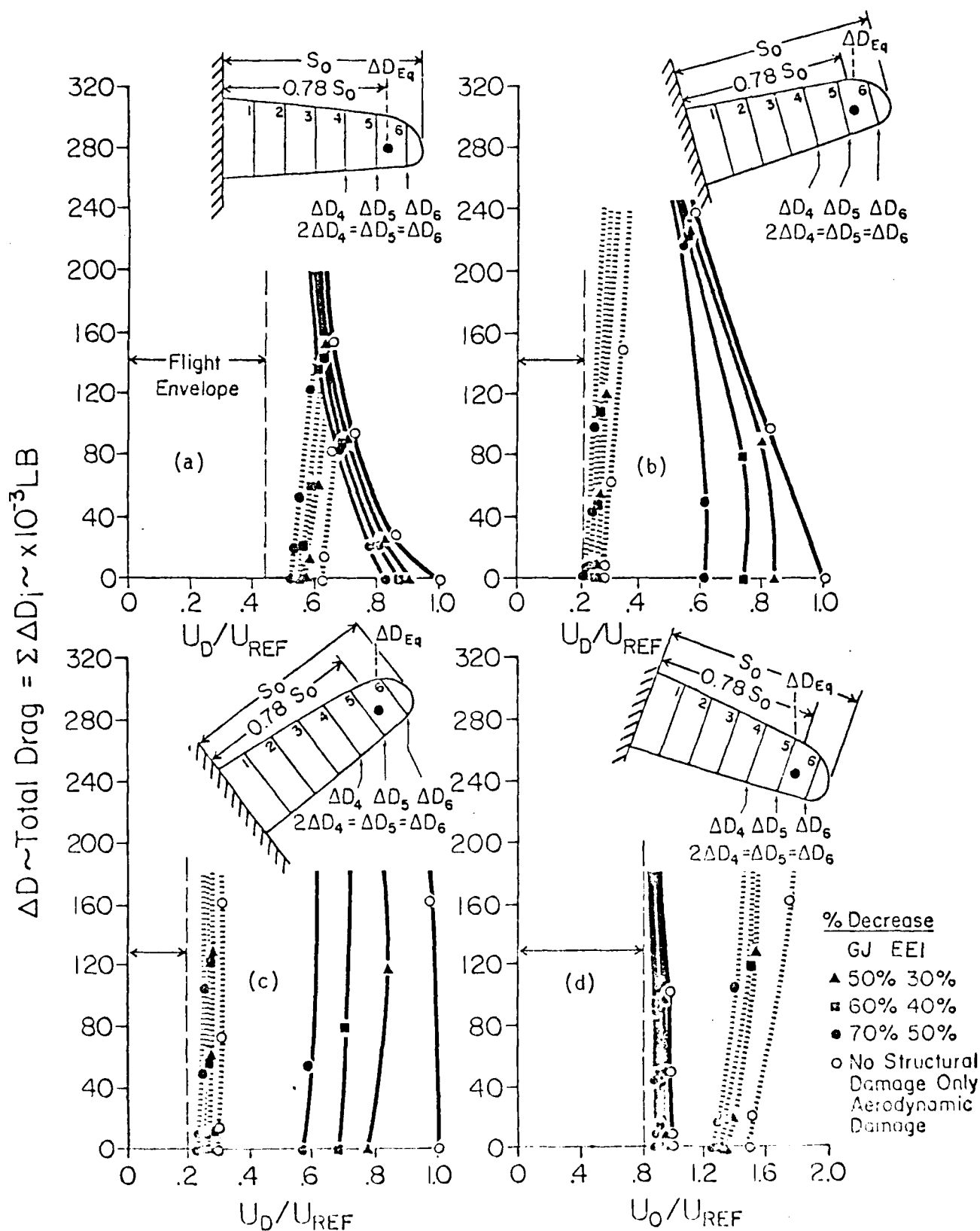


Figure 9



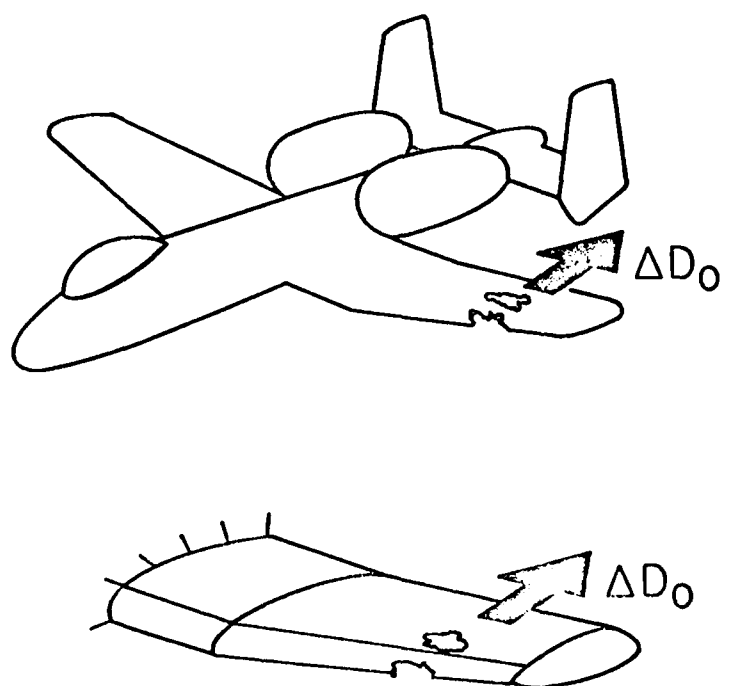
PROPOSED DAMAGE CLASSES

Figure 10



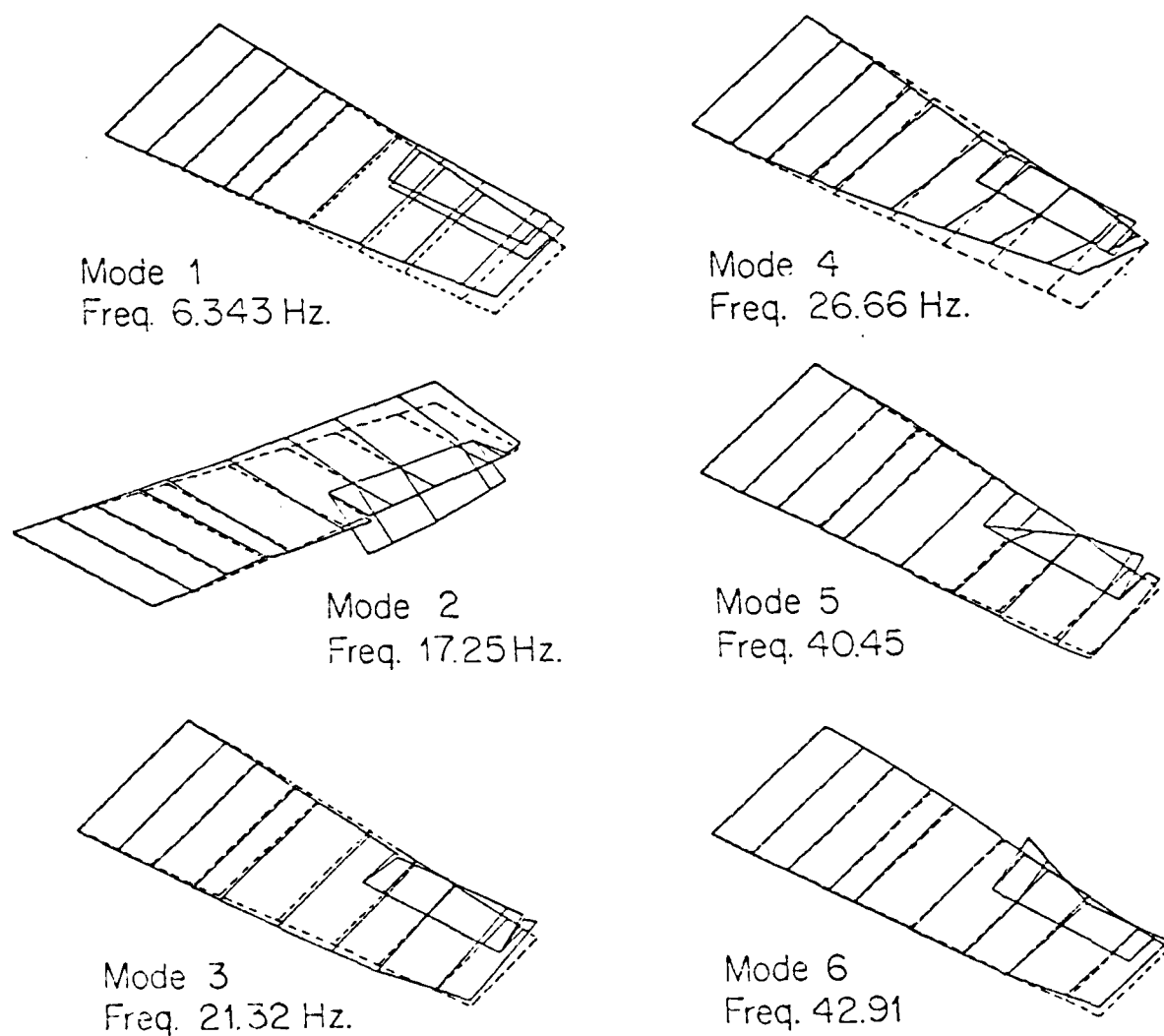
INFLUENCE OF MULTIPLE DAMAGE SITE DRAG
EFFECTS ON FLUTTER AND DIVERGENCE
OF FOUR SWEPT WING CONFIGURATIONS
(0°, 20°, 40° & -20°)

Figure 11



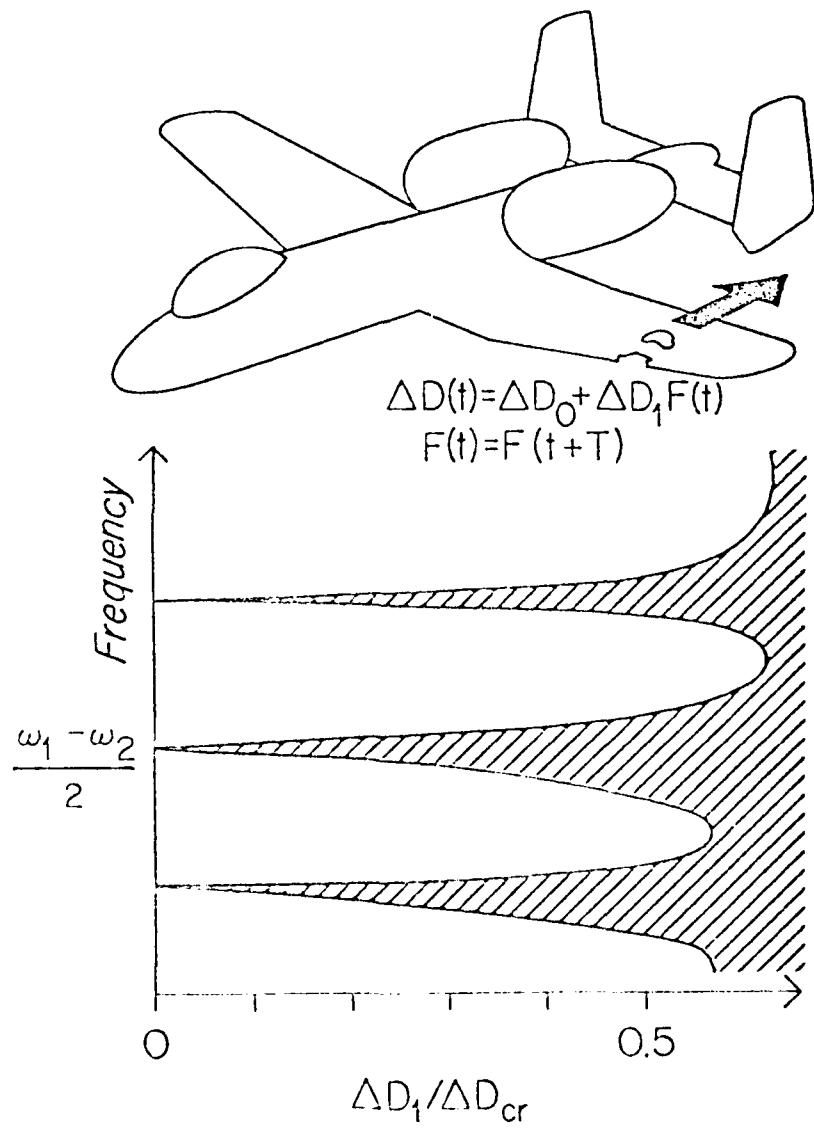
A-10 DRAG DIVERGENCE MODES

Figure 12



A-10 MODE SHAPES AND FREQUENCIES EMPLOYED IN THE DRAG DIVERGENCE MODELING

Figure 13



INFLUENCE OF TIME DEPENDENT DAMAGE INDUCED DRAG FORCE ON PROMOTING PARAMETRIC TYPE FLUTTER INSTABILITIES

Figure 14

PARAMETRIC INSTABILITIES INDUCED IN STATISTICAL FIGHTER
BY DAMAGE-INDUCED DRAG, PERIODIC IN TIME

Figure 15

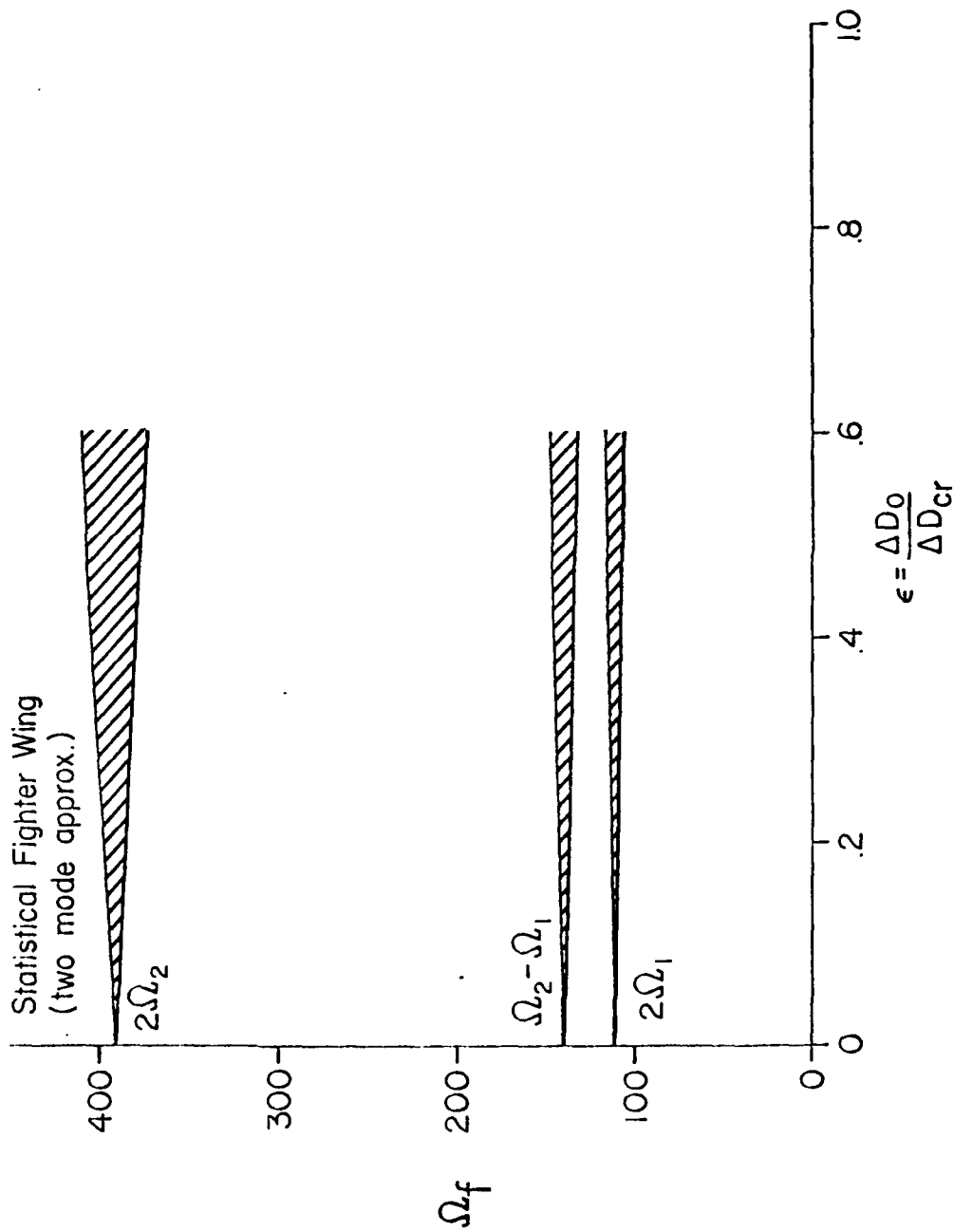


TABLE 1

STATISTICAL FIGHTER PROPERTIES DETERMINED AS
GEOMETRIC MEANS OF THE FOURTEEN DIFFERENT
FIGHTER AIRCRAFT

<u>Service Designation</u>	<u>Manufacturer</u>
P-51A	North American
XP-60	Curtiss-Wright
XP-84	Republic
XFJ-1	North American
XF8F-1	Grumman
XF9F-2	Grumman
F9F-3	Grumman
XFD-1	McDonnell
F2H-1	McDonnell
XF2D-1	McDonnell
XF6F-1	Grumman
XBT2D-1	Douglas
XF3D-1	Douglas
XF6U-1	Chance-Vought

Parameter X_g of typical fighter determined as geometric mean of similar parameters X_1, X_2, \dots etc. of above aircraft. That is,

$$X_g = (X_1 \cdot X_2 \cdot X_3 \dots X_m)^{1/m}$$

where X_1, X_2, \dots, X_m represent the set of variates. The specific typical wing parameters determined were

- Weight
- Static moment about a reference axis
- Bending area moment of inertia
- Mass moment of inertia about a reference axis
- Co-efficient of torsional rigidity
- Chord length
- Chordwise center of gravity position
- Chordwise elastic axis position

TABLE 2
TYPICAL DATA SHEET FOR DETERMINATION OF PARAMETERS FOR
REPRESENTATIVE AIRPLANE - CLASS I

STATION MODEL	Weight Distribution - Wing						W# W ₆ /W ₅
	1 W#	W ₁ /W ₅	2 W#	W ₂ /W ₅	3 W#	W ₃ /W ₅	
P-51A	539	9.38	454	7.90	271	4.71	153.
XP-60	964	7.90	636	5.21	411	3.37	337.
XP-84	7150	7.10	580	3.58	502	3.10	262.
XFJ-1	302	2.72	249	2.24	189	1.70	119.
XF8F-1	341	8.33	283	6.92	254	6.20	99.2
XF9F-2	431	5.20	287	3.46	107	1.29	90.8
F9F-2,3	365	3.48	311	2.96	140	1.33	111.
XFD-1	1158	16.1	314	4.37	121	1.68	80.
XF20-1	176	2.70	211	2.73	240	3.10	104.
F2H-1	398	2.86	543	3.91	545	3.92	187.
XF6F-1	510	5.63	508	5.61	419	4.63	185.
XBT2D-1	374	3.67	219	2.15	245	2.40	147
XF3D-1	445	4.08	497	4.56	392	3.60	169.
XF6U-1	407	6.24	230	3.53	129	1.98	83.8
REP. AIRPLANE	473	5.26	352	3.91	247	2.74	138.

W#
W₄/W₅

W#
W₅/W₄

W#
W₆/W₅

W#
W₆/W₅

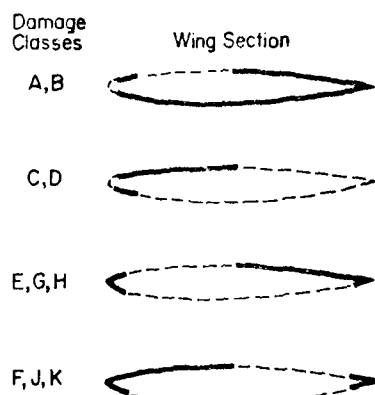
TABLE II Cont'd.
Wing Parameters - Representative Airplane - Class I

Parameter	1	2	3	4	5	6
Weight - #	473.	352.	247.	138.	90.	66.
$\frac{1}{2} \alpha_i - \# \text{ in.}^2 \cdot 10^{-4}$	25.8	15.6	8.78	4.81	2.855	1.73
$S_{a_i} - \# \text{ in.} \cdot 10^{-3}$	2.641	.728	1.133	.900	.536	.379
$Ei_i - \# \text{ in.}^2 \cdot 10^{-8}$	67.05	31.78	17.37	9.589	5.202	3.028
$GJ_i - \frac{\# \text{ in.}^2}{\text{rad}}$	10.8	46.4	26.9	12.25	8.85	4.98
Chord - in.	105.4	95.3	85.2	75.1	65.0	54.9
Elastic Axis - % Chord Aft of Leading Edge	33.6	33.6	33.6	33.6	33.6	33.6
Center of Gravity - % Chord Aft of Leading Edge	38.9	35.8	39.0	42.3	42.8	44.1
Front Spar - % Chord Aft of Leading Edge	26.8	26.8	26.8	26.8	26.8	26.8
Rear Spar - % Chord Aft of Leading Edge	61.5	61.5	61.5	61.5	61.5	61.5
Aileron Hinge Line - % Chord Aft of Leading Edge	76.2	76.2	76.2	76.2	76.2	76.2

S_0 = Semispan - 235 in.

TABLE 3.
KEY TO GENERALIZED DAMAGE CLASSES
(Taken from Reference 9)

Dashed lines in the sketches below indicate regions of possible hole damage. Projectile penetrates both regions of each sketch. These dashed lines do not indicate total skin damage, but locations of a family of possible projectile holes. Holes of class E & F damages have projecting skin; all other damages are flush holes.



Damage Classes	Hole Size *
A, C, E, F, G, J	.15c
B, D, H, K	.10c

* Diameter of an equal area circular hole

Digest of Drag Increases Due to Damage

Damage Class	Hole Size [†]	$M = .3$		$M = .7$		$M = .85$	
		$\frac{C_D}{\pi}^*$	P^*	$\frac{C_D}{\pi}^*$	P^*	$\frac{C_D}{\pi}^*$	P^*
A	.15c	1.2	6	2.4	10	3.4	
B	.10c	1.0	5	2.7	16	2.2	
C	.15c	.8	2.5	1.3	.3	-.7	
D	.10c	1.0	1	2.3	-1.5	-.5	
E	.15c	.2	6	1.0	9	1	
F	.15c	.2	.3	1.0	-.5	1	
G	.15c	-.2	4	0	6	-1	
H	.10c	0	4	0	7	-2.5	
J	.15c	-.2	.7	0	0	-1	
K	.10c	-.2	1	0	.5	-2.5	

† Diameter of an equal area circular hole

TABLE 4
DAMAGE INDUCED DRAG LEVELS FOR VARIOUS
MANEUVERING FLIGHT CONDITIONS

LOAD FACTOR <i>n</i>	C_L	C_D^* upper & lower bounds	$\Delta D \sim \text{LBS}$		
			2% hole	3% hole	5% hole
1	0.143	1.10 2.60	3,242# to 7,660#	4,863# to 11,492#	8,150# to 19,150#
5	0.713	3.54 7.48	10,433# to 22,040#	15,649# to 33,062#	26,080# to 55,100#
6	0.856	4.70 9.73	13,851# to 28,667#	20,777# to 43,000#	34,628# to 71,667#
6.5	0.927	5.30 11.0	15,619# to 32,400#	23,429# to 48,620#	39,048# to 81,033#

600 mph true maneuvering speed
20,000 ft. combat altitude

TABLE 5
FIRST SIX UNCOUPLED VIBRATIONAL MODES
NO STRUCTURAL DAMAGE

I. Bending Modes

	$\omega_1 = 55.849$	$\omega_2 = 188.314$	$\omega_3 = 450.217$ (rad/sec)
1.	1.7857E-2	-8.4490E-2	2.4423E-1
2.	8.1406E-2	-3.1113E-1	6.1549E-1
3.	2.0923E-1	-5.4403E-1	3.0448E-1
4.	4.1146E-1	-5.1329E-1	-7.5282E-1
5.	6.8315E-1	1.4467E-2	-9.5454E-1
6.	1.0000E+0	1.0000E+0	1.0000E+0

II. Torsional Modes

	$\omega_1 = 188.613$	$\omega_2 = 342.126$	$\omega_3 = 504.685$ (rad/sec)
1.	9.6133E-2	-1.8214E-1	2.4134E-1
2.	2.2696E-1	-3.3226E-1	2.2141E-1
3.	4.1644E-1	-3.2308E-1	-2.4823E-1
4.	6.4032E-1	-1.6795E-2	-5.9986E-1
5.	8.3951E-1	4.7194E-1	-1.4908E-1
6.	1.0000E+0	1.0000E+0	1.0000E+0

TABLE 6
FIRST SIX UNCOUPLED VIBRATIONAL MODES
EI-30%, GJ-50% DECREASED @ STA. 3,4,5

I. Bending Modes $f_i(x)$

$$\omega_1 = 52.640 \quad \omega_2 = 170.078 \quad \omega_3 = 407.619 \quad (\text{rad/sec})$$

1.	1.5054E-2	-7.9392E-2	-2.0984E-1
2.	6.8823E-2	-3.0221E-1	-3.5680E-1
3.	1.8015E-1	-5.6571E-1	-3.8472E-1
4.	3.7690E-1	-5.8070E-1	6.8730E-1
5.	6.6068E-1	-4.6049E-2	1.0000E+0
6.	1.0000E+0	1.0000E+0	-9.5720E-1

II. Torsional Modes $F_j(x)$

$$\omega_1 = 157.419 \quad \omega_2 = 292.544 \quad \omega_c = 421.626 \quad (\text{rad/sec})$$

1.	4.8591E-2	-1.7891E-1	1.9917E-1
2.	1.1817E-1	-3.6344E-1	2.8367E-1
3.	2.6572E-1	-5.1796E-1	-1.2760E-2
4.	5.6092E-1	-2.5312E-1	-7.7386E-1
5.	8.3818E-1	4.4114E-1	-1.6086E-1
6.	1.0000E+0	1.0000E+0	1.0000E+0

TABLE 7
FIRST SIX UNCOUPLED VIBRATIONAL MODES
EI-40%, GJ-60% DECREASED @ STA. 3,4,5

I. Bending Modes

	$\omega_1 = 51.127$	$\omega_2 = 163.074$	$\omega_3 = 389.939$ (rad/sec)
1.	1.3863E-2	-7.7807E-2	-1.9324E-1
2.	6.3465E-2	-2.9988E-1	-5.3870E-1
3.	1.6742E-1	-5.7621E-1	-4.0914E-1
4.	3.6138E-1	-6.1283E-1	6.4797E-1
5.	6.5057E-1	-7.5155E-2	1.0000E+0
6.	1.0000E+0	1.0000E+0	-9.1886E-1

II. Torsional Modes

	$\omega_1 = 148.836$	$\omega_2 = 286.953$	$\omega_3 = 406.357$ (rad/sec)
1.	4.2014E-2	-1.9661E-1	1.8453E-1
2.	1.0290E-1	-3.9334E-1	2.7817E-1
3.	2.4635E-1	-5.9470E-1	3.0931E-2
4.	5.8476E-1	-2.7798E-1	-8.3054E-1
5.	8.5998E-1	4.7952E-1	-4.3754E-2
6.	1.0000E+0	1.0000E+0	1.0000E+0

TABLE 8
FIRST SIX UNCOUPLED VIBRATIONAL MODES
EI-50%, GJ-70% DECREASED @ STA. 3,4,5

I. Bending Modes

	$\omega_1 = 49.225$	$\omega_2 = 155.417$	$\omega_3 = 369.508$ (rad/sec)
1.	1.2479E-2	-7.6342E-2	-1.7589E-1
2.	5.7220E-2	-2.9821E-1	-5.0725E-1
3.	1.5234E-1	-5.8956E-1	-4.3585E-1
4.	3.4278E-1	-6.5348E-1	6.0486E-1
5.	6.3849E-1	-1.1221E-1	1.0000E+0
6.	1.0000E+0	1.0000E+0	-8.8517E-1

II. Torsional Modes

	$\omega_1 = 132.217$	$\omega_2 = 264.400$	$\omega_3 = 361.831$ (rad/sec)
1.	2.8352E-2	-1.5937E-1	2.0050E-1
2.	7.0314E-2	-3.4021E-1	3.4743E-1
3.	1.8395E-1	-6.0422E-1	2.4247E-1
4.	5.2435E-1	-5.0652E-1	-9.5912E-1
5.	8.5386E-1	4.1558E-1	-9.4496E-2
6.	1.0000E+0	1.0000E+0	1.0000E+0

TABLE 9
 FIRST SIX UNCOUPLED VIBRATIONAL MODES
 EI-30%, GJ-50% DECREASED @ STA. 4,5,6

I. Bending Modes

$\omega_1 = 54.586$	$\omega_2 = 173.882$	$\omega_3 = 416.531$ (rad/sec)
1. 1.6462E-2	-7.5298E-2	-2.1644E-1
2. 7.5150E-2	-2.8411E-1	-5.7309E-1
3. 1.9354E-1	-5.2369E-1	-3.6521E-1
4. 3.8446E-1	-5.5831E-1	6.3126E-1
5. 6.6153E-1	-5.4452E-2	1.0000E+0
6. 1.0000E+0	1.0000E+0	-8.8978E-1

II. Torsional Modes

$\omega_1 = 169.266$	$\omega_2 = 288.424$	$\omega_3 = 426.189$ (rad/sec)
1. 5.2174E-2	-1.4506E-1	1.9416E-1
2. 1.2556E-1	-2.9697E-1	2.7157E-1
3. 2.3897E-1	-3.9974E-1	4.2939E-2
4. 4.4240E-1	-3.0187E-1	-5.9255E-1
5. 7.4149E-1	2.4940E-1	-6.3887E-1
6. 1.0000E+0	1.0000E+0	1.0000E+0

TABLE 10
 FIRST SIX UNCOUPLED VIBRATIONAL MODES
 EI-40%, GJ-60% DECREASED @ STA. 4,5,6

I. Bending Modes

$$\omega_1 = 53.959 \quad \omega_2 = 167.666 \quad \omega_3 = 403.325 \text{ (rad/sec)}$$

1.	1.5803E-2	-7.1950E-2	-1.9746E-1
2.	7.2194E-2	-2.7435E-1	-5.3308E-1
3.	1.8611E-1	-5.1696E-1	-3.7068E-1
4.	3.7132E-1	-5.7898E-1	5.5428E-1
5.	6.5072E-1	-8.6361E-2	1.0000E+0
6.	1.0000E+0	1.0000E+0	-8.1275E-1

II. Torsional Modes

$$\omega_1 = 160.891 \quad \omega_2 = 274.021 \quad \omega_3 = 400.230 \text{ (rad/sec)}$$

1.	4.0782E-2	-1.4069E-1	1.7509E-1
2.	9.8884E-2	-2.9552E-1	2.6964E-1
3.	1.9089E-1	-4.2316E-1	1.2086E-1
4.	3.7865E-1	-3.9885E-1	-4.9533E-1
5.	7.0805E-1	1.5313E-1	-8.0663E-1
6.	1.0000E+0	1.0000E+0	1.0000E+0

TABLE 11
FIRST SIX UNCOUPLED VIBRATIONAL MODES
EI-50%, GJ-70% DECREASED @ STA. 4,5,6

I. Bending Modes

$$\omega_1 = 53.143 \quad \omega_2 = 160.410 \quad \omega_3 = 388.571 \quad (\text{rad/sec})$$

1.	1.4980E-2	-6.8511E-2	-1.8581E-1
2.	6.8498E-2	-2.6448E-1	-5.1259E-1
3.	1.7681E-1	-5.1102E-1	-3.9055E-1
4.	3.5461E-1	-6.0478E-1	4.9183E-1
5.	6.3673E-1	-1.2608E-1	1.0000E+0
6.	1.0000E+0	1.0000E+0	-7.6730E-1

II. Torsional Modes

$$\omega_1 = 148.750 \quad \omega_2 = 257.867 \quad \omega_3 = 365.769 \quad (\text{rad/sec})$$

1.	2.8938E-2	-1.3573E-1	-1.5059E-1
2.	7.0883E-2	-2.9280E-1	-2.5832E-1
3.	1.3944E-1	-4.4553E-1	-2.0129E-1
4.	3.0350E-1	-5.2027E-1	3.1150E-1
5.	6.6726E-1	4.4689E-5	1.0000E+0
6.	1.0000E+0	1.0000E+0	-9.9149E-1

TABLE 12
FIRST SIX UNCOUPLED VIBRATIONAL MODES
EI-30%, GJ-50% DECREASED @ STA. 5,6

I. Bending Modes

	$\omega_1 = 55.593$	$\omega_2 = 183.106$	$\omega_3 = 425.207$ (rad/sec)
1.	1.7496E-2	-7.8475E-2	-2.1294E-1
2.	7.9785E-2	-2.9138E-1	-5.5685E-1
3.	2.0516E-1	-5.1869E-1	-3.3499E-1
4.	4.0470E-1	-5.1456E-1	6.1895E-1
5.	6.7315E-1	-3.6596E-2	1.0000E+0
6.	1.0000E+0	1.0000E+0	-9.1954E-1

II. Torsional Modes

	$\omega_1 = 181.590$	$\omega_2 = 302.679$	$\omega_3 = 443.677$ (rad/sec)
1.	6.8795E-2	-1.1984E-1	2.4890E-1
2.	1.6359E-1	-2.3870E-1	3.2321E-1
3.	3.0439E-1	-2.9968E-1	-2.0751E-2
4.	4.7818E-1	-1.9779E-1	-6.0198E-1
5.	7.0248E-1	1.7338E-1	-7.7613E-1
6.	1.0000E+0	1.0000E+0	1.0000E+0

TABLE 13
FIRST SIX UNCOUPLED VIBRATIONAL MODES
EI-40%, GJ-60% DECREASED @ STA. 5,6

I. Bending Modes

	$\omega_1 = 55.471$	$\omega_2 = 180.628$	$\omega_3 = 414.239$ (rad/sec)
1.	1.7324E-2	-7.5778E-2	-1.9813E-1
2.	7.9015E-2	-2.8248E-1	-5.2652E-1
3.	2.0322E-1	-5.0710E-1	-3.4169E-1
4.	4.0000E-1	-5.1463E-1	5.5501E-1
5.	6.6819E-1	-6.0867E-2	1.0000E+0
6.	1.0000E+0	1.0000E+0	-8.6903E-1

II. Torsional Modes

	$\omega_1 = 178.142$	$\omega_2 = 287.737$	$\omega_3 = 426.199$ (rad/sec)
1.	5.8882E-2	-1.0887E-1	-2.5879E-1
2.	1.4050E-1	-2.2316E-1	-3.6197E-1
3.	2.6315E-1	-3.0134E-1	-5.7188E-2
4.	4.1754E-1	-2.4928E-1	5.6523E-1
5.	6.4208E-1	6.6228E-2	1.0000E+0
6.	1.0000E+0	1.0000E+0	-9.5358E-1

TABLE 14
 FIRST SIX UNCOUPLED VIBRATIONAL MODES
 EI-50%, GJ-70% DECREASED @ STA. 5,6

I. Bending Modes

	$\omega_1 = 54.878$	$\omega_2 = 168.958$	$\omega_3 = 372.134$ (rad/sec)
1.	1.6500E-2	-6.4717E-2	-1.5806E-1
2.	7.5313E-2	-2.4579E-1	-4.4640E-1
3.	1.9392E-1	-4.5888E-1	-3.7213E-1
4.	3.8221E-1	-5.1422E-1	3.4990E-1
5.	6.4323E-1	-1.7061E-1	1.0000E+0
6.	1.0000E+0	1.0000E+0	-6.8870E-1

II. Torsional Modes

	$\omega_1 = 172.316$	$\omega_2 = 268.505$	$\omega_3 = 406.136$ (rad/sec)
1.	4.5928E-2	-1.0244E-1	-2.1376E-1
2.	1.1021E-1	-2.1720E-1	-3.2250E-1
3.	2.0863E-1	-3.1783E-1	-1.2443E-1
4.	3.3641E-1	-3.2135E-1	3.8566E-1
5.	5.5348E-1	-8.4158E-2	1.0000E+0
6.	1.0000E+0	1.0000E+0	-6.7547E-1

TABLE 15
CRITICAL SPEEDS FOR DAMAGED WING
AERODYNAMIC DAMAGE SITE AT 60% SEMI-SPAN

1. No Structural Damage

divergence speed mph	D 1bs	flutter speed mph	D 1bs
1470	0	950	0
1239	25,678	968	15,673
1134	43,021	990	32,789
983	80,735	1133	107,254
870	126,609	—	—

2. EI-30%, GJ-50% Decreased @ STA. 3,4,5

divergence speed mph	D 1bs	flutter speed mph	D 1bs
1165	0	734	0
1025	17,574	748	9,359
837	58,592	820	56,236
748	93,689	—	—

TABLE 15 CONT'D

3. EI-40%, GJ-60% Decreased @ STA. 3,4,5

divergence speed mph	D 1bs	flutter speed mph	D 1bs
1098	0	690	0
969	15,715	701	8,224
794	52,700	768	49,305
711	84,464	—	—

4. EI-50%, GJ-70% Decreased @ STA. 3,4,5

divergence speed mph	D 1bs	flutter speed mph	D 1bs
957	0	588	0
865	12,515	596	5,941
723	43,682	640	34,228
651	70,912	—	—

TABLE 16
CRITICAL SPEEDS FOR DAMAGED WING
AERODYNAMIC DAMAGE SITE AT 80% SEMI-SPAN

1. No Structural Damage

divergence speed mph	D 1bs	flutter speed mph	D 1bs
1470	0	950	0
1151	22,160	980	16,065
1038	36,050	1040	35,911
887	65,830	—	—
785	102,950	—	—

2. EI-30%, GJ-50% Decreased @ STA. 4,5,6

divergence speed mph	D 1bs	flutter speed mph	D 1bs
1234	0	784	0
1010	17,060	808	10,918
794	52,730	—	—
708	83,850	—	—
643	138,320	—	—

TABLE 16 CONT'D

3. EI-40%, GJ-60% Decreased @ STA. 4,5,6

divergence speed mph	D 1bs	flutter speed mph	D 1bs
1150	0	731	0
955	15,255	748	9,358
758	48,074	—	—
678	76,797	—	—
620	128,600	—	—

4. EI-50%, GJ-70% Decreased @ STA. 4,5,6

divergence speed mph	D 1bs	flutter speed mph	D 1bs
1040	0	650	0
883	13,041	673	7,576
709	42,060	—	—
638	68,090	—	—
588	115,670	—	—

TABLE 16 CONT'D

5. EI-70%, GJ-70% Decreased @ STA. 4,5,6

divergence speed mph	D 1bs	flutter speed mph	D 1bs
1040	0	649	0
865	12,256	668	7,309
687	39,470	—	—
615	63,266	—	—
564	106,420	—	—

TABLE 17
CRITICAL SPEEDS FOR DAMAGED WING
AERODYNAMIC DAMAGE SITE AT 90% SEMI-SPAN

1. No Structural Damage

divergence speed mph	D 1bs	flutter speed mph	D 1bs
1470	0	950	0
1029	17,711	1040	18,090
913	27,887	1850	114,512
776	50,363	—	—
699	81,682	—	—

2. EI-30%, GJ-50% Decreased @ STA.5,6

divergence speed mph	D 1bs	flutter speed mph	D 1bs
950	15,096	940	14,780
725	43,961	—	—
667	74,374	—	—

TABLE 17 CONT'D

3. EI-40%, GJ-60% Decreased @ STA. 5,6

divergence speed mph	D 1bs	flutter speed mph	D 1bs
1302	0	839	0
917	14,065	912	13,912
703	41,333	—	—
653	71,285	—	—

4. EI-50%, GJ-70% Decreased @ STA. 5,6

divergence speed mph	D 1bs	flutter speed mph	D 1bs
1226	0	789	0
872	12,719	864	12,487
674	37,994	—	—
634	67,197	—	—

TABLE 17 CONT'D

5. EI-70%, GJ-70% Decreased @ STA. 5,6

divergence speed mph	D 1bs	flutter speed mph	D 1bs
1226	0	789	0
857	12,285	864	12,487
659	36,322	—	—
621	65,819	—	—

TABLE 18
FIRST SIX COUPLED VIBRATION MODES
NO STRUCTURAL DAMAGE

First Mode $\omega_1 = 55.626$ (rad/sec)

1.	1.7861E-2	8.1218E-5
2.	8.1424E-2	2.0540E-4
3.	2.0927E-1	4.3005E-4
4.	4.1153E-1	7.5596E-4
5.	6.8321E-1	1.0918E-3
6.	1.0000E+0	1.4170E-3

Second Mode $\omega_2 = 184.114$ (rad/sec)

1.	-7.0912E-2	-2.3049E-3
2.	-2.5918E-1	-5.3055E-3
3.	-4.4617E-1	-9.3808E-3
4.	-3.9579E-1	-1.2708E-2
5.	9.8291E-2	-1.3433E-2
6.	1.0000E+0	-1.1905E-2

TABLE 18 CONT'D
FIRST SIX COUPLED VIBRATION MODES
NO STRUCTURAL DAMAGE

Third Mode $\omega_3 = 201.391$ (rad/sec)

1.	1.1515E-1	-1.3058E-2
2.	4.4077E-1	-3.0717E-2
3.	8.3226E-1	-5.5749E-2
4.	1.0000E+0	-8.6347E-2
5.	7.0826E-1	-1.1601E-1
6.	-1.5209E-2	-1.4203E-1

Fourth Mode $\omega_4 = 355.122$ (rad/sec)

1.	5.3731E-3	2.1714E-2
2.	-3.0053E-2	3.8287E-3
3.	-1.3595E-1	3.3356E-2
4.	-1.9454E-1	-5.9493E-3
5.	1.2846E-1	-5.9137E-2
6.	1.0000E+0	-1.0816E-1

TABLE 18 CONT'D
FIRST SIX COUPLED VIBRATION MODES
NO STRUCTURAL DAMAGE

Fifth Mode $\omega_5 = 429.720$ (rad/sec)

1.	-2.5510E-1	-3.2359E-3
2.	-6.5983E-1	-1.2928E-3
3.	-3.9736E-1	8.6078E-3
4.	6.5964E-1	2.1318E-2
5.	1.0000E+0	5.4350E-4
6.	-6.3645E-1	-6.5914E-2

Sixth Mode $\omega_6 = 542.953$ (rad/sec)

1.	6.0846E-2	-2.6348E-2
2.	1.9756E-1	-1.8475E-2
3.	5.7742E-2	3.6184E-2
4.	-5.4663E-1	5.0145E-2
5.	-6.3671E-1	-4.8803E-3
6.	1.0000E+0	-7.3730E-2

TABLE 19
 FIRST SIX COUPLED VIBRATIONAL MODES
 EI-30%, GJ-50% DECREASE @ STA. 5,6

First Mode $\omega_1 = 55.327$ (rad/sec)

1.	1.7494E-2	7.9823E-5
2.	7.9777E-2	2.0194E-4
3.	2.0515E-1	4.2304E-4
4.	4.0369E-1	7.4481E-4
5.	6.7315E-1	1.1935E-3
6.	1.0000E+0	1.8490E-3

Second Mode $\omega_2 = 179.263$ (rad/sec)

1.	-7.1562E-2	-1.6471E-3
2.	-2.6485E-1	-3.7713E-3
3.	-4.6860E-1	-6.6213E-3
4.	-4.5350E-1	-8.5789E-3
5.	9.1557E-3	-7.8630E-3
6.	1.0000E+0	-2.1363E-3

TABLE 19 CONT'D
FIRST SIX COUPLED VIBRATIONAL MODES
EI-30%, GJ-50% DECREASE@ STA. 5,6

Third Mode $\omega_3 = 193.045$ (rad/sec)

1.	8.6587E-2	-1.4718E-2
2.	3.4417E-1	-3.4806E-2
3.	6.9724E-1	-6.3928E-2
4.	9.7189E-1	-1.0011E-1
5.	1.0000E+0	-1.4886E-1
6.	7.0264E-1	-2.1636E-1

Fourth Mode $\omega_4 = 320.403$ (rad/sec)

1.	-5.0885E-2	1.7111E-2
2.	-1.9085E-1	3.3200E-2
3.	-3.0635E-1	3.8754E-2
4.	-2.1647E-1	2.1283E-2
5.	2.1238E-1	-3.0627E-2
6.	1.0000E+0	-1.3863E-1

TABLE 19 CONT'D
 FIRST SIX COUPLED VIBRATIONAL MODES
 EI-30%, GJ-50% DECREASE @ STA.5,6

Fifth Mode $\omega_5 = 388.648$ (rad/sec)

1.	-2.2937E-1	-1.0620E-2
2.	-6.1366E-1	-1.4671E-2
3.	-4.4284E-1	-2.2136E-3
4.	5.1701E-1	2.9144E-2
5.	1.0000E+0	4.3232E-2
6.	-7.7407E-1	-5.5731E-2

Sixth Mode $\omega_6 = 503.248$ (rad/sec)

1.	1.3173E-1	-2.0362E-2
2.	3.5538E-1	-2.1157E-2
3.	1.4274E-1	1.5050E-2
4.	-6.4707E-1	4.6765E-2
5.	-8.9515E-1	3.6104E-2
6.	1.0000E+0	-6.7133E-2

TABLE 20
 FIRST SIX COUPLED VIBRATIONAL MODES
 EI-40%, GJ-60% DECREASE @ STA. 5,6

First Mode

$$\omega_1 = 55.188 \text{ (rad/sec)}$$

1.	1.7319E-2	7.9137E-5
2.	7.8994E-2	2.0024E-4
3.	2.0319E-1	4.1957E-4
4.	3.9996E-1	7.3922E-4
5.	6.6816E-1	1.2272E-3
6.	1.0000E+0	2.0493E-3

Second Mode

$$\omega_2 = 176.679 \text{ (rad/sec)}$$

1.	-7.2892E-2	-1.3041E-3
2.	-2.7157E-1	-2.9632E-3
3.	-4.8737E-1	-5.1405E-3
4.	-4.9189E-1	-6.2855E-3
5.	-4.4556E-2	-4.2758E-3
6.	1.0000E+0	5.2893E-3

TABLE 20 CONT'D
FIRST SIX COUPLED VIBRATIONAL MODES
EI-40%, GJ-60% DECREASE @ STA. 5,6

Third Mode

$$\omega_3 = 189.298 \text{ (rad/sec)}$$

1.	4.9298E-2	-1.2555E-2
2.	2.0447E-1	-2.9741E-2
3.	4.4459E-1	-5.4864E-2
4.	7.0332E-1	-8.6123E-2
5.	9.0890E-1	-1.3226E-1
6.	1.0000E+0	-2.0698E-1

Fourth Mode

$$\omega_4 = 305.886 \text{ (rad/sec)}$$

1.	-6.4990E-2	1.5677E-2
2.	-2.3483E-1	3.1442E-2
3.	-3.6645E-1	4.0023E-2
4.	-2.5528E-1	3.0011E-2
5.	2.0585E-1	-1.5284E-2
6.	1.0000E+0	-2.5528E-1

TABLE 20 CONT'D
 FIRST SIX COUPLED VIBRATIONAL MODES
 EI-40%, GJ-60% DECREASE @ STA. 5,6

Fifth Mode

$$\omega_5 = 375.809 \text{ (rad/sec)}$$

1.	-2.1571E-1	-1.2203E-2
2.	-5.8362E-1	-1.8276E-2
3.	-4.4140E-1	-7.2774E-3
4.	4.7227E-1	2.6343E-2
5.	1.0000E+0	5.5392E-2
6.	-8.4272E-1	-4.4001E-2

Sixth Mode

$$\omega_6 = 488.413 \text{ (rad/sec)}$$

1.	1.5159E-1	-1.8832E-2
2.	4.0575E-1	-2.1748E-2
3.	1.8497E-1	8.8428E-3
4.	-6.6586E-1	4.2804E-2
5.	-9.9924E-1	5.0966E-2
6.	1.0000E+0	-6.5087E-2

TABLE 21
FIRST SIX COUPLED VIBRATIONAL MODES
EI-50%, GJ-70% DECREASE @ STA. 5,6

First Mode $\omega_1 = 55.006$ (rad/sec)

1.	1.7095E-2	7.8320E-5
2.	7.7996E-2	1.9821E-4
3.	2.0069E-1	4.1547E-4
4.	3.9520E-1	7.3273E-4
5.	6.6164E-1	1.2742E-3
6.	1.0000E+0	2.3780E-3

Second Mode $\omega_2 = 172.753$ (rad/sec)

1.	-7.8181E-2	-6.9945E-4
2.	-2.9435E-1	-1.5207E-3
3.	5.4007E-1	-2.4379E-3
4.	-5.7986E-1	-1.9211E-3
5.	-1.4871E-1	3.4304E-3
6.	1.0000E+0	2.4021E-2

TABLE 21 CONT'D
 FIRST SIX COUPLED VIBRATIONAL MODES
 EI-50%, GJ-70% DECREASE @ STA.5,6

Third Mode

 $\omega_3 = 183,658$ (rad/sec)

1.	-5.3312E-4	-6.9230E-3
2.	1.0440E-2	-1.6429E-2
3.	6.5776E-2	-3.0463E-2
4.	2.1757E-1	-4.7805E-2
5.	5.1705E-1	-7.6013E-2
6.	1.0000E+0	-1.3159E-1

Fourth Mode

 $\omega_4 = 286.639$ (rad/sec)

1.	-7.8687E-2	1.4291E-2
2.	-2.8112E-1	2.9797E-2
3.	-4.4222E-1	4.1693E-2
4.	-3.3011E-1	4.0233E-2
5.	1.6070E-1	6.8471E-3
6.	1.0000E+0	-1.4465E-1

AD-AD91 674

TEXAS UNIV AT AUSTIN DEPT OF AEROSPACE ENGINEERING AN--ETC F/6 1/3
THE EFFECTS OF WARHEAD-INDUCED DAMAGE ON THE AEROELASTIC CHARAC--ETC(U)
JUL 80 J H CHANG, R O STEARMAN AFOSR-78-3569

UNCLASSIFIED

AFOSR-TR-80-1039 NL

2 of 2
4D A
131674

END
DATE FILMED
12-80
DTIC

TABLE 21 CONT'D
 FIRST SIX COUPLED VIBRATIONAL MODES
 EI-50%, GJ-70% DECREASE @ STA. 5,6

Fifth Mode

$$\omega_5 = 361.625 \text{ (rad/sec)}$$

1.	-1.9899E-1	-1.3638E-2
2.	-5.4501E-1	-2.1904E-2
3.	-4.3189E-1	-1.3350E-2
4.	4.2563E-1	2.0836E-2
5.	1.0000E+0	6.7331E-2
6.	-9.1850E-1	-2.8823E-2

Sixth Mode

$$\omega_6 = 469.745 \text{ (rad/sec)}$$

1.	-1.5485E-1	1.4987E-2
2.	-4.1473E-1	1.9435E-2
3.	-2.1788E-1	-1.5291E-3
4.	6.0003E-1	-3.1527E-2
5.	1.0000E+0	-5.9862E-2
6.	-8.7734E-1	5.3384E-2

TABLE 22

The Influence of Coupled and Uncoupled
 Vibrational Modes used on Critical Speed
 for Aerodynamic Site At 90% Semi-Span
 with 0° Sweep

1. No structural damage

divergence speed mph		flutter speed mph	
A	B	A	B
1470	1485	950	920
1029	1030	1050	965
776	777	—	—
699	677	—	—

2. EI 30%, GJ 50% Structural damage

divergence speed mph		flutter speed mph	
A	B	A	B
950	953	940	895
725	728	—	—
667	670	—	—

NOTE: A Uncoupled vibration modes used ϕ .

B Coupled vibration modes used.

TABLE 22 CONT'D

3. EI 40%, GJ-60% Structural damage

divergence speed mph		flutter speed mph	
A	B	A	B
1302	1299	839	816
917	920	912	867
703	707	—	—
653	654	—	—

4. EI 50%, GJ 70% Structural damage

divergence speed mph		flutter speed mph	
A	B	A	B
1226	1242	789	770
872	874	864	820
674	679	—	—
634	636	—	—

TABLE 22 CONT'D

5. EI 70%, GJ 70% Structural damage

divergence speed mph		flutter speed mph	
A	B	A	B
1226	1183	780	770
857	866	864	823
657	665	—	—
621	625	—	—

APPENDIX A
ESTIMATE OF DRAG INCREMENTS DUE TO DAMAGE

A.1 Introduction

During the course of this study it became evident that the current state of the art for estimating damage induced drag levels leaves much to be desired. For the estimation of the influence of aerodynamic damage on the performance, the drag rise should be evaluated on the basis of constant lift in order to simulate the lift required to maintain desired flight conditions. This basis may cause an over-estimation of the drag in the present study of aeroelastic failure. Here, possible reduction in lift should also be considered in the analysis, by estimating the drag rise on the basis of fixed angle of attack. Actual damage will generally require aileron deflection to overcome possible asymmetries in the rolling moments generated by the two halves of the wing. This asymmetry depends on the loss in lift due to the aerodynamic damage and its location. A drag increment based on fixed angle of attack takes into account the loss in lift and is believed to be a low bound since it does not include the lift associated with the aileron deflection. The two estimates for ΔC_D due to damage are shown schematically in Figure A.1. It is believed that the actual case lies between estimates based on fixed lift coefficients and fixed angle of attack. A better estimate cannot be made at the present stage of the study, since the required aerodynamic data is lacking.

A.2 Estimate of Drag Increment Due to Aerodynamic Damage

The first systematic experimental investigation of the aerodynamic characteristics of damaged wings is a Cornell Aeronautical Laboratory report (11) dated 1952. The test model was a 24" chord wing, with NACA 65,012 airfoil, that spanned the 102" height of the test section. The wing was tested at Mach numbers 0.3, 0.7 and 0.85 with various simulated damage configurations that are shown in Figure A.2 which is Table I of Reference 11.

The test results were processed in a later report by the same laboratory (9) by fitting a parabolic drag model to the data. Using the notation of this reference:

$$C_D = C_{D_\pi} + p C_L^2,$$

changes of C_D caused by damage are recorded as changes of the "parasitic" drag coefficient, C_{D_π} , and the slope $p = dC_D/dC_L^2$. The results were normalized to the damage hole area, instead of wing area by introducing

$$\begin{aligned} C_D^* &= -\frac{\Delta D}{qA} \\ &= C_{D_\pi}^* + p^* C_L^2 \end{aligned}$$

Figure A.3, which is Table II of Reference 9, is a summary of drag increases due to damage holes of various configurations. This data is the basis for the estimations made in Section 3, 4 and 5.

Before we proceed and discuss the results of this investigation it is important to make notes on some special features of the test conditions. First, the basic wing is two-dimensional, thus the slope p^* in the expression for C_D^* should not be interpreted as induced drag in the sense of a finite wing. Secondly, the airfoil had a thickness ratio of 12% which was typical of aircraft of the time of the study. This value is much higher than the thickness ratios of 6% or less used on most contemporary fighters. This difference is of importance since transonic phenomena are much more violent for the thick airfoil. For example, it shows a dip in the lift curve slope at a Mach number about 0.85, an early drag divergence and steeper drag rise (12). The Mach number 0.85 tests were executed only over a very narrow range of angles of attack, namely over very small values of lift coefficients. Therefore, the slope term, p^* , was not evaluated for this Mach number. The discussion below will, therefore, be limited to $M = 0.7$. The investigation included several configurations with edges of the holes raised to form a "scoop" or a "spoiler" lip. The height of the lips were $1/2"$ and $1"$, or about 2% and 4% of the local chord. Naturally, such protuberances generate a considerable drag. However, according to information received, actual petals on battle damaged wings of high performance fighters do not exceed $1"$ which is only a fraction of 1% of full size typical chord. Some care should, therefore, be utilized when applying damage cases E & F of Figure A.2.

The damage configurations that gave the highest drag rise

are 1A15-2A15 and 1A10-2A10. Recall from Figure A.2 that hole locations 1 and 2 are at the leading edge and at quarter chord upper surface. It is believed that the combination of a leading edge hole which acts as an inlet, a hollow wing that serves as a settling chamber and a hole located in the region of maximum suction generate a fountain which acts on the external flow as a spoiler that causes separation and the associated drag rise. For example, for damage configuration 1A15-2A15 we find

A/S = 0.00415 and

$$C_{D\pi}^* = 2.4, \quad p^* = 10.0$$

which give for a fixed $C_L = 0.8$ a drag rise of $C_D^* = 8.8$ or its equivalent $\Delta C_D = 0.036$. The alternative estimate, namely the one based on fixed angle of attack, predicts increase in drag coefficient is 0.017 which is less than half the value predicted for constant C_L .

A through hole is represented by damage configuration 2A15-4A15 whose two holes are centered at quarter chord. For this configuration

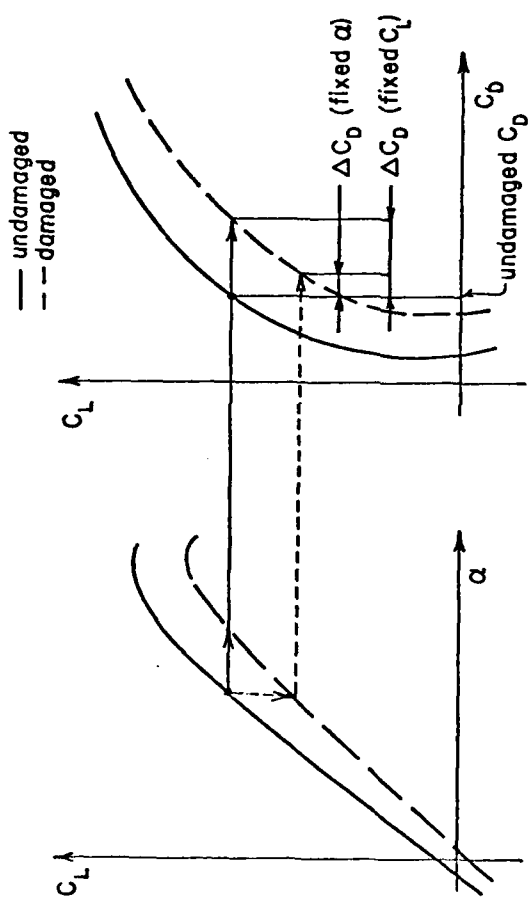
$$C_{D\pi}^* = 0 \quad p^* = 6$$

For $C_L = 0.8$ the predicted increase in drag coefficient is $C_D^* = 3.84$ or $\Delta C_D = 0.016$. For the case of constant angle of attack we find for the damaged wing at $\alpha = 4.6^\circ$, $C_L = 0.64$ and $C_D = 0.028$, i.e. an increase of $\Delta C_D = 0.006$ which again is less than half the value predicted for fixed C_L .

To conclude the analysis of Reference 11 and 9, we summarize findings for $C_L = 0.8$ (undamaged) and $M = 0.7$.

CONFIGURATION	REPRESENTING	C_D^*		ΔC_D	
		fixed C_L	fixed α	fixed C_L	fixed α
1A15-2A15	Leading edge inlet forms a fountain	8.8	4.1	.036	.017
2A15-4A15	Through hole at quarter chord	3.8	1.5	.016	.006

However, we recall that these values are not necessarily valid in transonic speeds, that they do not include the expected large change in induced drag which results from the modification in lift distribution and that they do not include the additional effects associated with aileron deflection that should follow any non-symmetrical damage.



TWO WAYS TO ESTIMATE DRAG RISE DUE TO DAMAGE

Figure A.1

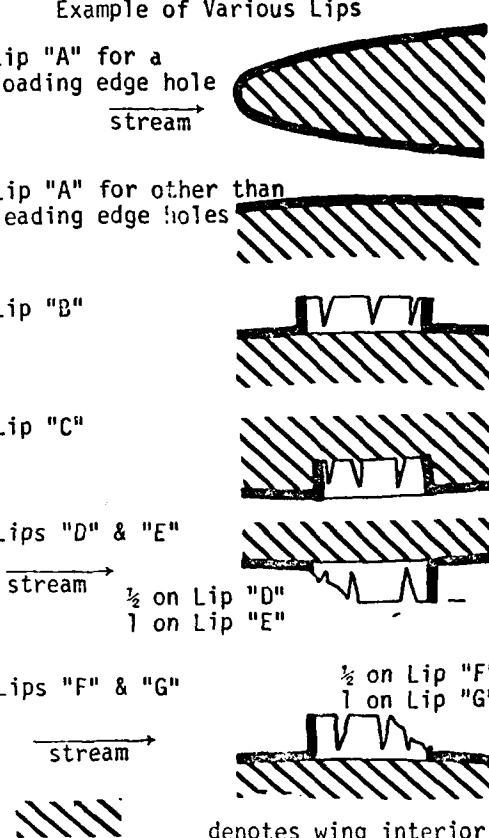
Table I
Key to Configuration Notation

Hole Location			Example of Various Lips
<u>Hole Number</u>	<u>Location</u>		
1	Leading edge		Lip "A" for a loading edge hole stream
2	.25 chord, upper surface		
3	.70 chord, upper surface		
4	.25 chord, lower surface		
5	.70 chord, lower surface		

Lip Configuration		
<u>Symbol</u>	<u>Type of Lip</u>	<u>Depth of Flange</u>
A	flush	none
B	protruding	1/2 in.
C	receding	1/2 in.
D	scoop	1/2 in.
E	scoop	1 in.
F	spoiler	1/2 in.
G	spoiler	1 in.

Description of Hole Size		
<u>Numerical</u>	<u>Hole Diameter*</u>	
10	.10 chord	
15	.15 chord	

*For leading edge holes, the diameter of an equal area circular hole.



DAMAGE CONFIGURATIONS TESTED IN REFERENCE 11

Figure A.2

M = .30		M = .70		M = .85	
CONFIG. C_{Q_1}	C_{Q_2}	CONFIG. C_{D_1}	C_{D_2}	CONFIG. C_{D_1}	C_{D_2}
1A15-2A15	1.2	6.0	2A15-3A15	-.5	1.9
	1.9	0		0	0
1A15-2A15	.7	3.8	2A15-4A15	-.1	5.0
	1.9	6.0		0	9.0
1A10-2A10	1.0	5.0	2A15-5A15	-.5	3.4
	0	.7		2.7	16.0
1A10-3A10	1.0	3.3	3A15-5A15	-.1	1.4
	0	1.4		2.2	0
2B15-4C15	.1	9.0	2A10-3A10	-.5	2.0
	1.0	1.6		.7	10.0
2B15-5C15	.2	7.0	2A10-4A10	1.1	4.9
	0	4.3		1.2	10.0
2E15-4G15	.2	2.5	2A10-5A10	.5	4.0
	7.5	2.0		1.2	8.0
2E15-5G15	.5	2.5	3A10-5A10	0	0
	.7	0		0	0
1A15-2A15	2.4	10.0	2A15-3A15	0	2.9
					0
1A15-3A15	1.0	.7	2A15-4A15	0	6.0
		0			9.0
1A10-2A10	2.7	16.0	2A15-5A15	0	6.0
					0
1A10-3A10	2.2	0	3A15-5A15	0	0
					0
2B15-4C15	.7	10.0	2A10-3A10	0	3.8
					-1.6
2B15-5C15	1.0	9.0	2A10-4A10	0	10.0
					-1.6
2E15-4G15	1.2	8.0	2A10-5A10	0	9.8
					3.8
2E15-5G15	1.0	8.0	3A10-5A10	0	0
					0

Note: Values of p^* are given in pairs. The upper figure of each pair is for $\alpha > 0$; the lower for $\alpha < 0$.

SUMMARY OF DRAG INCREASES ATTRIBUTABLE TO DAMAGE HOLES IN WINGS

Figure A.3

APPENDIX B

PROBLEM FORMULATION

The classical thin beam buckling equations employed in the present analyses were first developed by Michell and are currently derived in many classical texts on structural analysis (13). The math model utilized for the present study is illustrated in Figure 4. Here the reference axes are taken along the elastic axis of the wing which may be at an angle of sweep Λ and a root chord angle of attack α_0 relative to the on-coming flow. In addition, the damage is assumed to be localized giving rise to modifications in the aerodynamic loads that can be represented as localized changes in drag, lift, and moment. These concentrated changes, illustrated in Figure 2, are referenced to chordwise coordinate η forward or aft of the elastic axis and spanwise coordinate ξ . Writing the equilibrium equations in the deformed state of the wing yields:

$$\begin{aligned} EI)_1 \frac{d^2\eta}{d\xi^2} &= M_\xi \approx EI)_1 \frac{d^2v}{dx^2} \\ EI)_2 \frac{d^2\zeta}{d\xi^2} &= -M_\eta \approx EI)_2 \frac{d^2\omega}{dx^2} \\ GJ)_{\text{eff}} \frac{d\theta}{d\xi} &= M_\xi \approx GJ)_{\text{eff}} \frac{d\beta}{dx} . \end{aligned} \quad (1B)$$

For fighter wing configurations the chordwise stiffness is much greater than the stiffness normal to the chord direction, i.e.

$$\frac{EI)_1}{EI)_2} \gg 1$$

and the last two equations essentially uncouple, to the first order, from the first one. This is due to the smallness of the chordwise deflection η and its lower order derivatives when compared to the wing twist θ and deflection ζ normal to the wing chord plane. That is, for the small angles and deflections occurring at the onset of a flutter or divergence instability

$$\eta \approx v \quad \zeta \approx w \quad \theta \approx \beta$$

with β projection of θ on y-z plane

v projection of η on y-z plane

w projection of ζ on y-z plane

and deflections along the x axis are neglected. Further simplifications can be made upon assuming curvatures in $\eta\xi$ and $\zeta\xi$ planes are very nearly equal to the curvatures in the xy and zx planes respectively and also that

$$\frac{d\theta}{d\xi} \approx \frac{d\beta}{dx} .$$

Displacements are also considered small (flutter or divergence just initiated) cosines of all angles are equal to unity and sines of all angles are equal to the angle and its tangent. Bending moments and torques in the cross section of the deformed configuration can be referenced to the original coordinate state by the following transformation

$$\begin{Bmatrix} M_\xi \\ M_\eta \\ M_\zeta \end{Bmatrix} = \begin{bmatrix} 1 & \partial v / \partial y & \partial w / \partial x \\ -\partial v / \partial y & 1 & \beta \\ -\frac{\partial w}{\partial x} & -\beta & 1 \end{bmatrix} \begin{Bmatrix} M_x \\ M_y \\ M_z \end{Bmatrix} \quad (2B)$$

Now the moments M_x , M_y , and M_z created by the damage induce aerodynamic forces are from Figure 4.

$$\begin{aligned} M_x = & -\Delta D \cos \Lambda [\omega(\xi) + \eta \beta(\xi) - \omega(x)] \\ & - \Delta L [v(\xi) + \eta - v(x) - \eta \frac{\partial v}{\partial x}] + \Delta M \end{aligned}$$

$$\begin{aligned} M_y = & \Delta D \sin \Lambda [\omega(\xi) + \eta \beta(\xi) - \omega(x)] \\ & + \Delta L [(\xi - x) - \eta \frac{\partial v}{\partial x}(\xi)] \end{aligned} \quad (3B)$$

$$\begin{aligned} M_z = & \Delta D \cos \Lambda [(\xi - x) - \frac{\partial v}{\partial \xi}(\xi) \eta] \\ & - \Delta D \sin \Lambda [v(\xi) + \eta - v(x)] \end{aligned}$$

Taking the appropriate derivatives of the second and third equations of 1B provides, along with 2B:

$$\frac{d^2}{dx^2} \left[EI \frac{d^2\omega}{dx^2} \right] + \frac{d^2 M_y}{dx^2} + \frac{d^2}{dx^2} [\beta M_z] = L \quad (4B)$$

$$- \frac{d}{dx} \left[GJ \frac{d\beta}{dx} \right] + \frac{d}{dx} [M_x] + \frac{d}{dx} \left[M_z \frac{\partial\omega}{\partial x} \right] = M$$

where L and M are the distributed lift and moment on the lifting surface.

Coupling (3B) and (4B) gives rise to damage induced lift and moment terms dropping out as higher order effects, while only the damaged induced drag terms are remaining. This result is also based upon the observations from wind tunnel tests that ΔL and ΔD are roughly of the same order. At large angles of attack α_0 the change in lift term ΔL , which is usually negative, may contribute a small amount to the chordwise drag force tending to diverge the wing. For moderate to small angles of attack, however, this effect is small and the equations take the form:

$$- \frac{d}{dx} \left[GJ \frac{d\beta}{dx} \right] + S_a \frac{\partial^2 \omega}{\partial t^2} + I_\alpha \frac{\partial \beta}{\partial t^2} + \Delta D \cos \Lambda (\xi - x) \frac{\partial^2 \omega}{\partial x^2} - \Delta D \sin \Lambda \eta \frac{\partial \omega}{\partial x^2} = M$$

$$\frac{d^2}{dx^2} \left[EI \frac{d^2\omega}{dx^2} \right] + m \frac{\partial^2 \omega}{\partial t^2} + S_a \frac{\partial^2 \beta}{\partial t^2} - \Delta D \sin \Lambda \frac{d^2 \omega}{dx^2} - 2\Delta D \cos \Lambda \frac{d\beta}{dx} + \Delta D \cos \Lambda (\xi - x) \frac{d^2 \beta}{dx^2} - \Delta D \Lambda \eta \sin \Lambda \frac{d^2 \beta}{dx^2} = L$$

The above constitutes the basic equations employed for the flutter and divergence analyses of the present study.

APPENDIX C

THREE-DIMENSIONAL FINITE ELEMENT MODELING OF STRUCTURAL DISCONTINUITIES IN CONSTANT CHORD WINGS OR ROTOR ELEMENTS

To illustrate the detail in finite element structural modeling that can be accomplished for a well defined structure, reference is made here to an earlier investigation of structural discontinuities on constant chord rotors or wings with a single cell torque box. The study is also an alternate check on the influence that localized structural damage has on the mode shape frequency characteristics of undamaged wings or rotors.

A three-dimensional finite element model of a typical composite rotor blade has been developed in Reference 20 to investigate the influence of structural repair discontinuities reflected in the blade's stiffness and modal characteristics. Modern computational procedures including multi-level substructuring (Reference 21) are employed during the solution of symmetric finite element equations. The computed stiffness and modal characteristics of the blade are correlated to those obtained from laboratory tests. Also included in this report are the results of the preliminary investigations of the influence of idealized repair discontinuities as reflected by the finite element model.

As can be seen in Figure C1-a, the rotor blade is fairly uniform in cross-section along its entire length of 22 ft. with the exception of the additional grip plates and doublers overlaid on the 4 ft. portion at

the supported end. During the laboratory tests, the blade was mounted on a relatively rigid support fixture.

In the finite element model, the blade was assumed to have constant cross-sectional properties within two spanwise regions as shown in Fig. C1-b. The difference between these regions is due to the fact that thicker membrane elements were required near the support so that the effect of the grip plates and doublers (Fig. C1-a) could be reflected in the idealization. As shown in Fig. C1-c, three-dimensional brick elements were used to model the spar and the honeycomb core while membrane elements were used for the skin. The typical section in each spanwise region has 21 elements (9 bricks and 12 membrane elements) and 44 nodal points (Fig. C1-c). The total finite element idealization (Fig. 22) consists of 88 of these typical sections each being assumed to have identical stiffness and mass properties within each spanwise region. This results in 1848 elements and 1958 nodal points with three degrees-of-freedom at each node.

The reduction process, which is a simultaneous static and Guyan reduction of stiffness and mass matrices, respectively, takes advantage of the repeated use of identical substructures (Ref. 21). First the 21 elements of Fig. C1-c were processed in each spanwise region to produce two of the 88 substructures of Fig. 3. Subsequently two of these substructures were combined in each region to generate two of the 44 substructures of Fig. C4. This process was applied two more times to produce the substructures of Fig. C5 and C6. The 11 elements of Fig. C6 were then combined to generate the final substructure having 30 nodal points as shown in Fig. C7.

The stiffness and mass matrices of the final substructures (Fig. C7) were then used to determine the flexibility and modal characteristics of the rotor blade. Fig. C8 depicts the correlation of the measured (Ref. 22) and computed flexibility coefficients corresponding to the vertical deflection of the blade under the applied unit loads as shown in the figure. The discrepancy was less than 1.5 percent. Table C-1 gives the correlation of the measured (Ref. 23) and computed natural frequencies of the blade. Also included in this table are the computed frequencies from a beam model (Ref. 23) that requires predetermined cross-sectional, stiffness, and mass characteristics of the blade. Although the finite element model gave larger discrepancies than the beam model for the out-of-plane bending modes in this particular case, it could be found attractive for the geometric generality it provides in the idealization of local structural discontinuities such as holes, repairs, stiffeners, etc.

Currently, the influences of the three types of damage shown in Fig. C-9 on the stiffness and modal characteristics of the blade have been investigated as a preliminary study of more general repair discontinuities. The first two damage types, i.e. HOLE and NOTCH, result from complete delamination of the core and skin on both faces of the blade adjacent to the leading edge torque box as shown in Fig. C9-a and C9-b. In this study, the spanwise location for these damages has been selected to be at STA 75 or 213 inches from the tip. The third damage, i.e. CRACK, is formed by the delamination of the skin on both faces and located between STA 72 and STA 264 as shown in Fig. C9-c. This damage idealizes the separation of the leading edge torque box from the trailing edge torque box as a result of longitudinal cracking of the skin on both faces of the blade.

The effect of the above types of damage on the flexibility of the blade is shown in Fig. C10. The load-deflection figures shown in this figure, which could be considered a computer simulation of the droop test, correspond to computed tip deflections of the blade under upward applied forces at STA 288. The deflection values and percent changes in the deflection due to the damage are given in Table C-2 for all stations considered in the standard droop test.

The computed natural frequency response of the damaged blades are given in Table C-3 for the first five vibration modes. Also included in this table is the percent change in the vibration frequencies due to the damage.

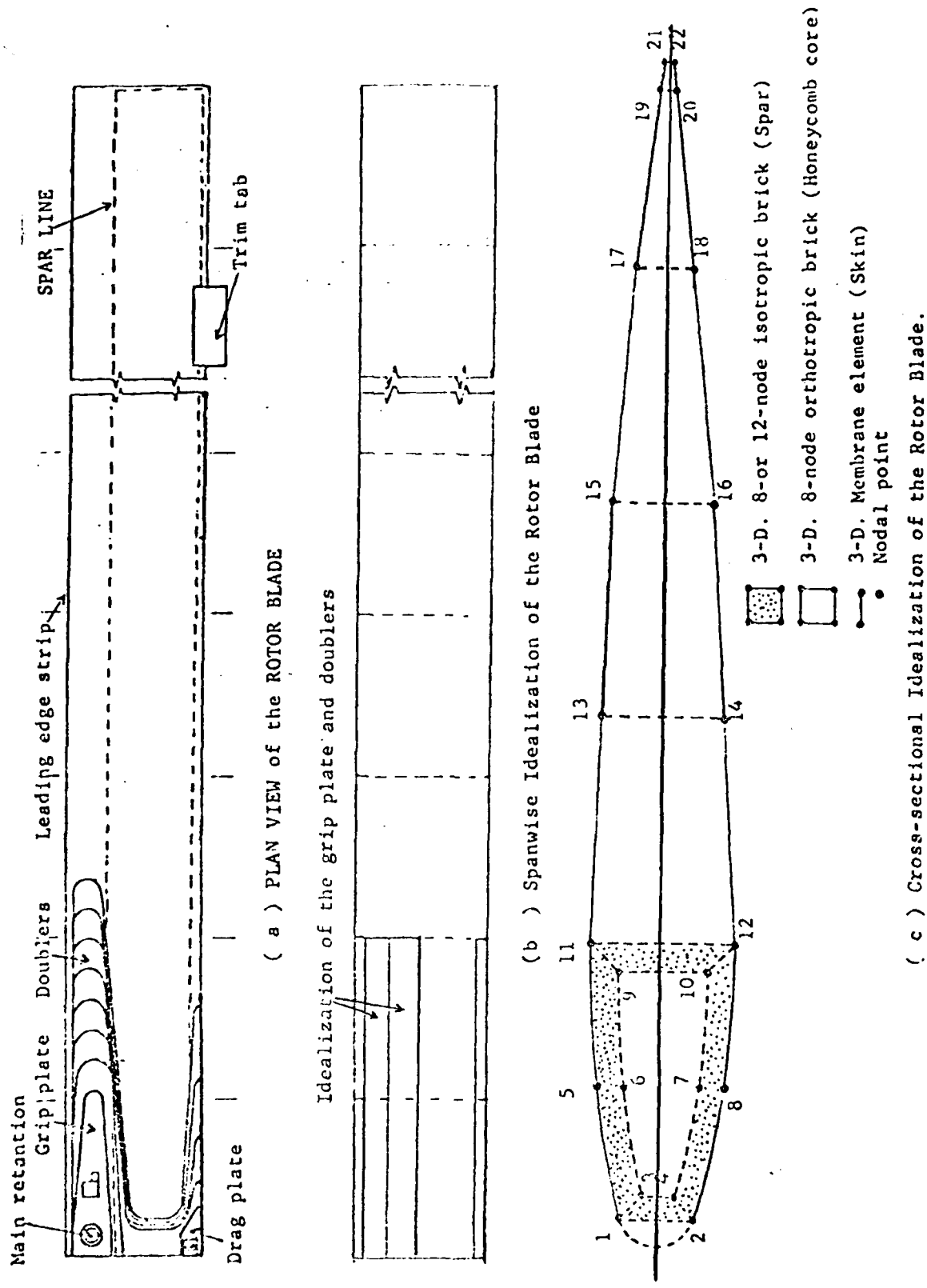
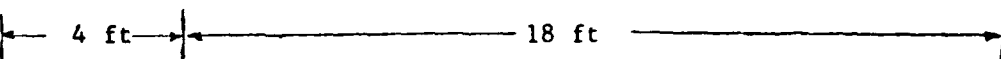


Figure 6-1. Finite Element Idealization of the Rotor Blade.

Region 1.



Region 2.

18 ft



Fig. C-2. Plan View Showing the Two Typical Cross-Sections.

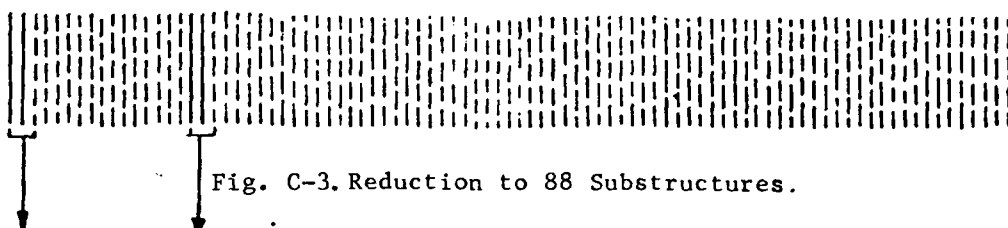


Fig. C-3. Reduction to 88 Substructures.

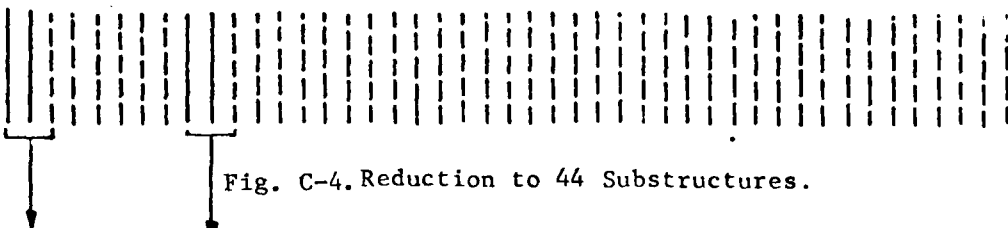


Fig. C-4. Reduction to 44 Substructures.

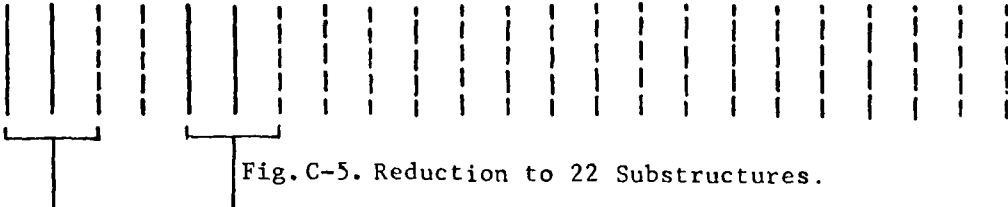


Fig. C-5. Reduction to 22 Substructures.

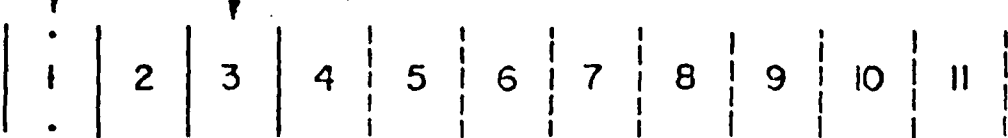


Fig. C-6. Reduction to 11 Substructures.

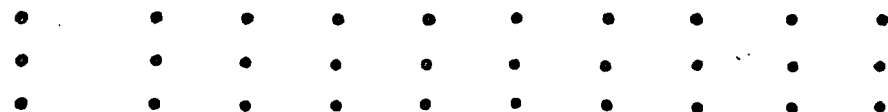
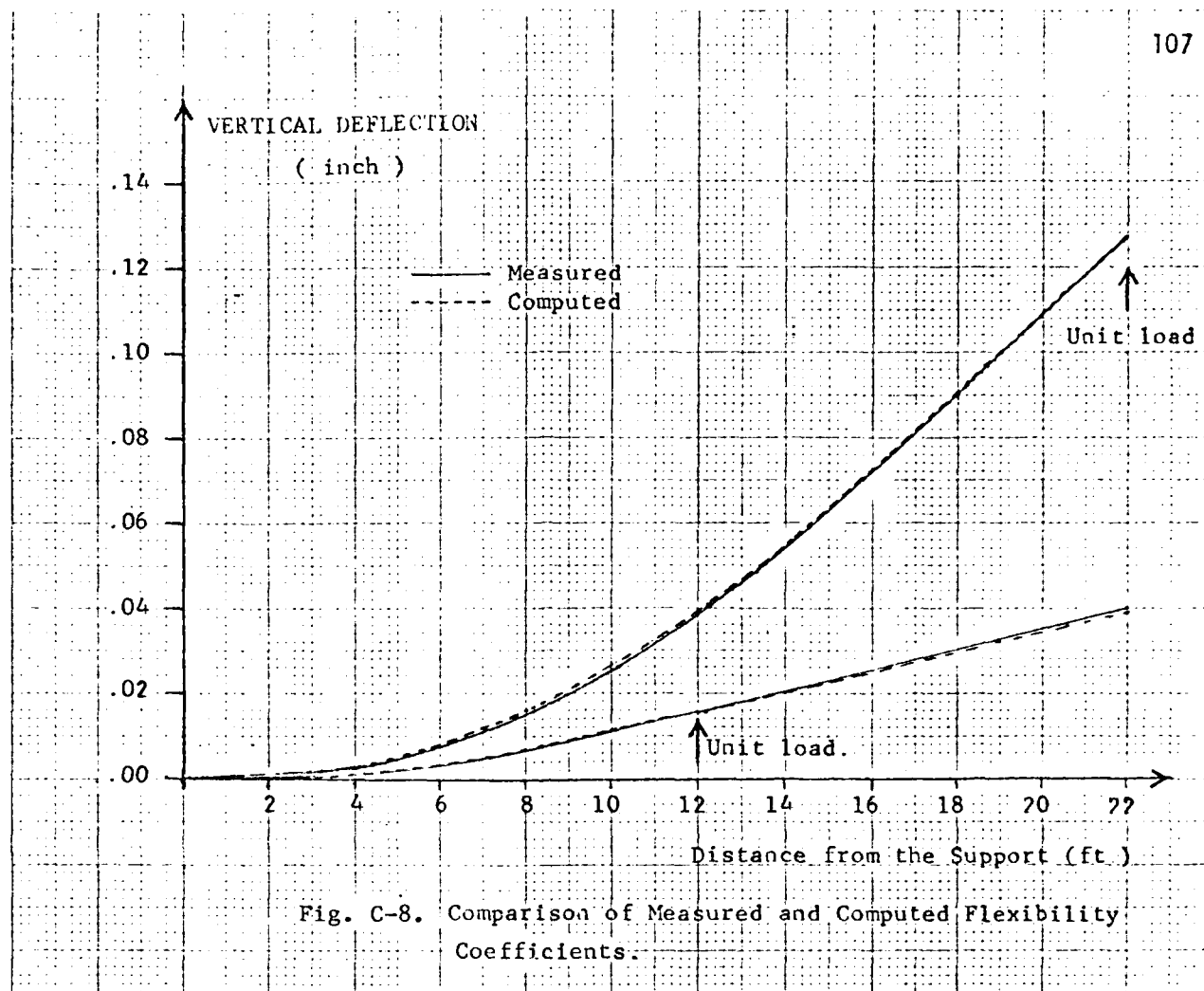


Fig. C-7. Reduction to Final Substructure with 30 Nodes



BLADE MODE	Experimental Frequency HZ	Computed Freq & % Discrepancy			
		DF1758 (Ref. 3) HZ	%	Finite Element HZ	%
First Out-of-Plane		1.44		1.37	
First In-Plane	6.0	6.32	5.3	6.30	5.0
Second Out-of-Plane	8.1	8.05	0.6	8.29	2.3
Third Out-of-Plane	19.9	20.88	4.9	22.15	11.3
First Torsion	26.0	26.45	1.7	26.02	0.1

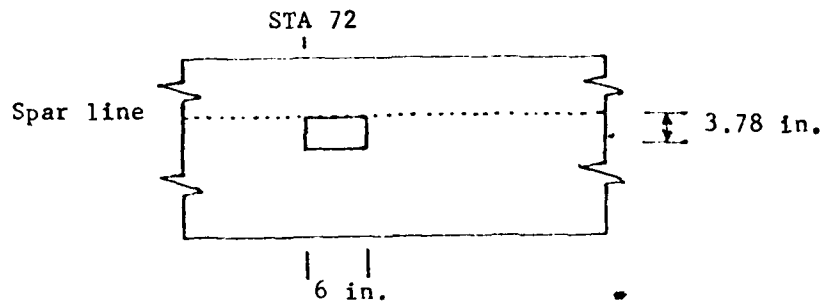
Table C-1. - Correlation of Calculated and Measured Natural Frequencies.

BLADE STATION	Computed Deflection and % Change in Deflection							
	UN-DAMAGED		HOLE		NOTCH			
	inch	%	inch	inch	%	inch	%	
STA 288	12.73	0	12.82	0.71	13.06	2.59	13.44	5.58
STA 240	6.51	0	6.57	0.92	6.73	3.38	6.85	5.22
STA 192	2.77	0	2.80	1.08	2.88	3.97	2.90	4.69
STA 144	0.86	0	0.87	1.16	0.90	4.65	0.89	3.49

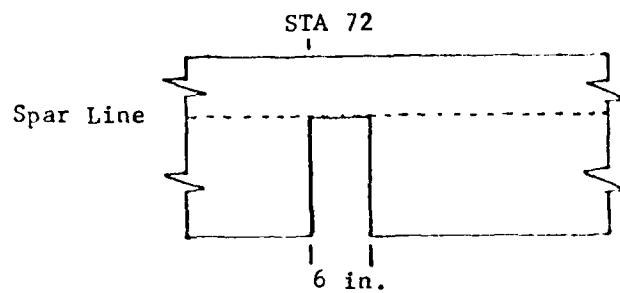
Table C-2. The Effect of the Idealized Damages on the Flexibility of the Rotor Blade.(Note that 100 lbs.applied at STA 288.)

BLADE MODE	Computed Frequencies (HZ) and % Change of Frequency							
	UN-DAMAGED		HOLE		NOTCH			
	HZ	%	HZ	%	HZ	%		
First Out-of-Plane	1.367	0	1.361	0.44	1.345	1.61	1.349	1.32
First In-Plane	6.299	0	6.295	0.06	3.749	40.48	6.319	0.32
Second Out-of-Plane	8.295	0	8.286	0.11	8.263	0.39	8.226	0.83
Third Out-of-Plane	22.153	0	22.170	0.08	22.191	0.17	21.953	3.61
First Torsion	26.019	0	25.914	0.40	25.471	2.11	24.105	7.36

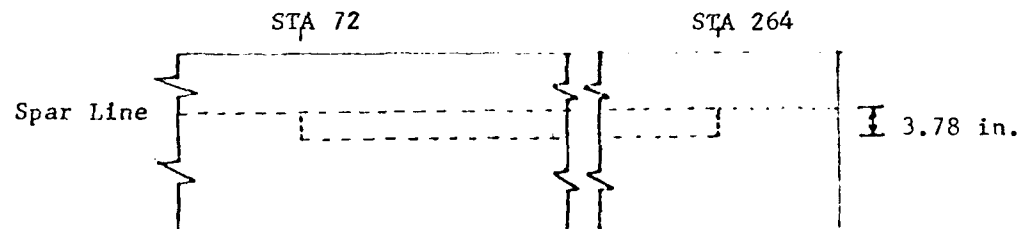
Table C-3. - The Effect of Idealized Damages on the Natural Frequencies of the Blade.



(a) HOLE : Delamination of core and skin on both faces.



(b) NOTCH : Delamination of core and skin on both faces.



(c) CRACK : Delamination of skin on both faces.

Fig. C-9.- Idealized Damage Types.

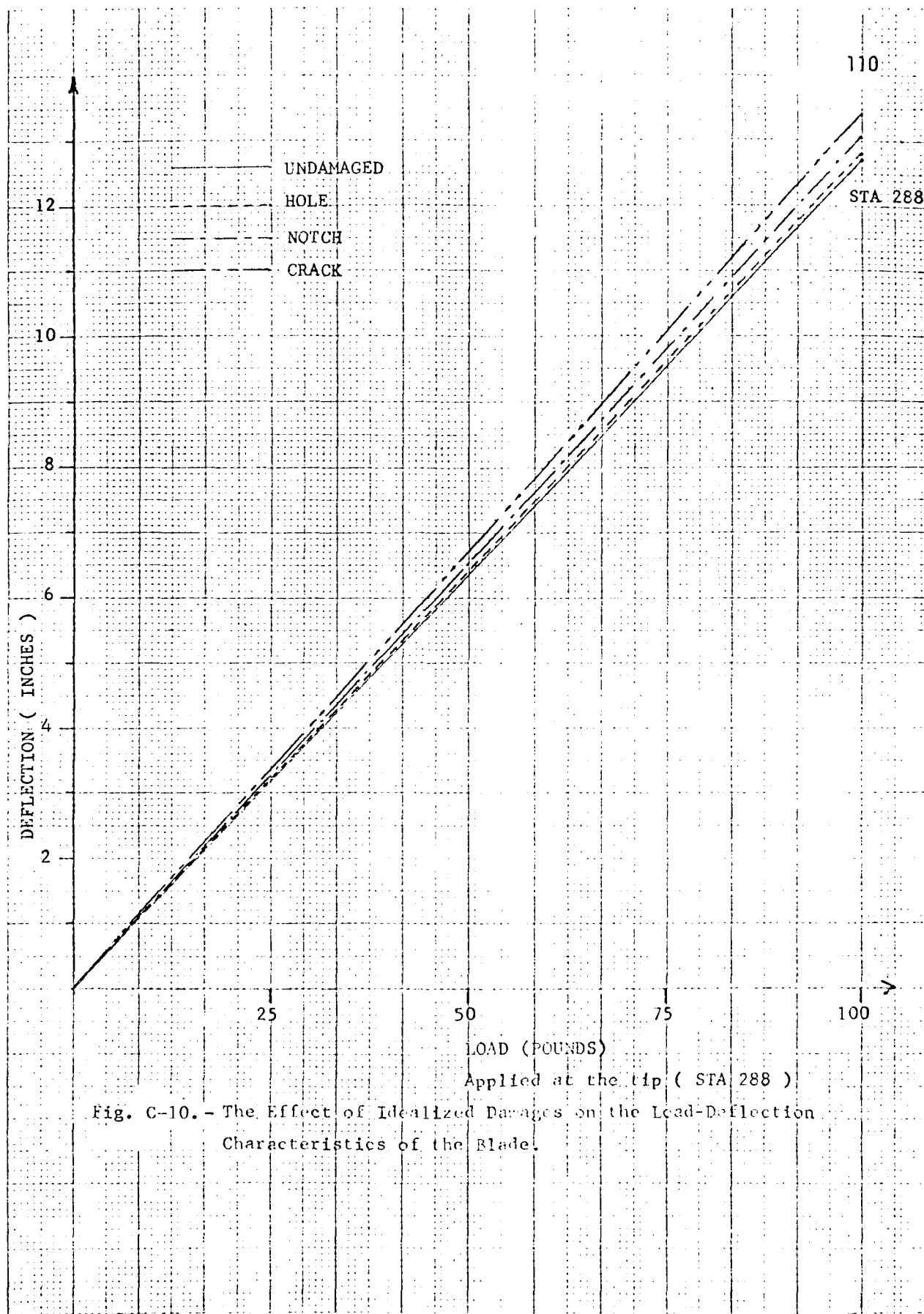


Fig. C-10. - The Effect of Idealized Damages on the Load-Deflection Characteristics of the Blade.